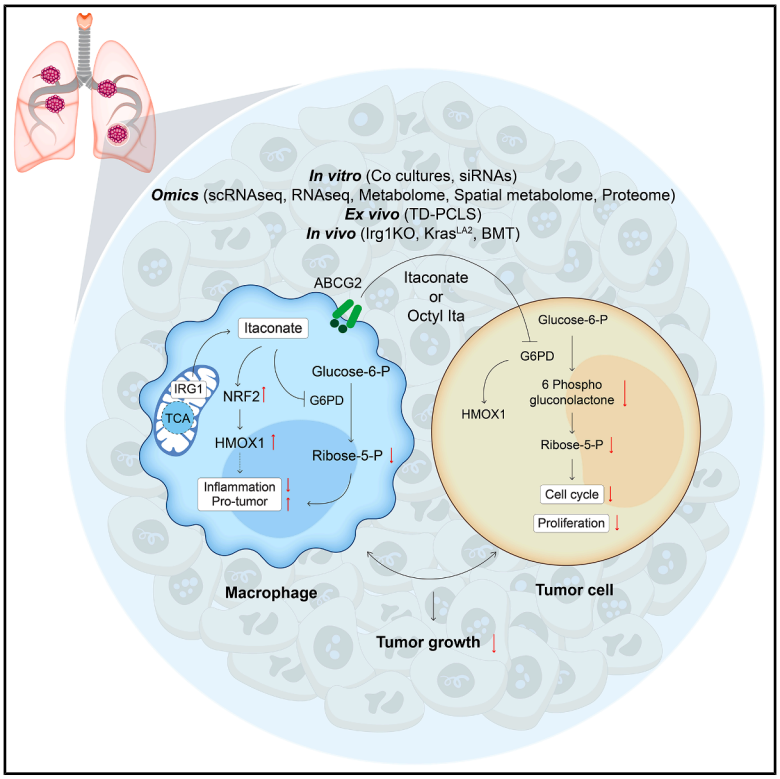
Cell Metabolism

Article

IRG1/itaconate rewires macrophage and lung tumor metabolism through G6PD inhibition

Graphical abstract



Highlights

- Spatial metabolomics reveals itaconate depletion within lung tumors
- IRG1/itaconate suppresses lung tumor growth via metabolic reprogramming
- Octyl itaconate directly inhibits lung cancer proliferation and reprograms macrophages
- Itaconate inhibits G6PD and reduces pentose phosphate pathway flux

Authors

Siavash Mansouri, Golnaz Hesami, Anoop Ambikan, ..., Werner Seeger, Soni Savai Pullamsetti, Rajkumar Savai

Correspondence

savai.rajkumar@innere.med.uni-gieesen.de

In brief

Mansouri et al. show that IRG1-derived itaconate is spatially depleted in lung tumors and that restoring it with octyl itaconate suppresses tumor growth. Mechanistically, itaconate inhibits G6PD activity and pentose phosphate pathway flux, reprograms macrophages toward anti-tumor states, and directly limits lung cancer cell proliferation.

Mansouri et al., 2026, Cell Metabolism *38*, 1460–1477
July 7, 2026 © 2026 The Author(s). Published by Elsevier Inc.
https://doi.org/10.1016/j.cmet.2026.05.005

CellPress

CellPress
OPEN ACCESS

Cell Metabolism

Article

IRG1/itaconate rewires macrophage and lung tumor metabolism through G6PD inhibition

Siavash Mansouri,[1,2] Golnaz Hesami,[1,2] Anoop Ambikan,[3] Annika Karger,[1,2] Stephan Klatt,[4] Ujjwal Neogi,[3] Konda Babu Kurakula,[5] Blerina Aliraj,[6] Anne Miller,[7] Boryana Petrova,[8] Miloslav Sanda,[9,10,11] Evelyn Sirait-Fischer,[6,18] Stefan Guenther,[2] Carsten Kuenne,[2] Clemens Ruppert,[12] Ibrahim Alkoudmani,[13] Stefan Gattenlöhner,[14] Sven Zukunft,[4] Ingrid Fleming,[4] Arvand Haschemi,[15] Thorsten Stiewe,[1,16] Friedrich Grimminger,[1,12] Martin Reck,[17] Andreas Weigert,[6,18] Werner Seeger,[1,2,12] Soni Savai Pullamsetti,[1,2,12,19] and Rajkumar Savai[1,2,12,19,20,*]

[1]Institute for Lung Health (ILH), Justus Liebig University, Giessen, Germany
[2]Max Planck Institute for Heart and Lung Research, German Center for Lung Research (DZL), Cardio-pulmonary Institute (CPI), Bad Nauheim, Germany
[3]The Systems Virology Lab, Division of Clinical Microbiology, Department of Laboratory Medicine, Karolinska Institutet, Stockholm, Sweden
[4]Institute for Vascular Signalling, Centre for Molecular Medicine, Goethe University, Frankfurt, Germany
[5]Department of Physiology, Amsterdam Cardiovascular Sciences, Amsterdam University Medical Center, Free University Medical Center, Amsterdam, the Netherlands
[6]Goethe University Frankfurt, Faculty of Medicine, Institute of Biochemistry I, Frankfurt, Germany
[7]Center for Pathobiochemistry and Genetics, Medical University of Vienna, Vienna, Austria
[8]Department of Core Facilities, Medical University of Vienna, Vienna, Austria
[9]Max Planck Institute for Heart and Lung Research, DZHK German Centre for Cardiovascular Research, Partner Site Rhine-Main, Cardio-Pulmonary Institute (CPI), Bad Nauheim, Germany
[10]Clinical and Translational Glycoscience Research Center, Georgetown University, Washington, DC 20057, USA
[11]Department of Oncology, Lombardi Comprehensive Cancer Center, Georgetown University, Washington, DC 20057, USA
[12]Department of Internal Medicine, DZL, CPI, Justus Liebig University, Giessen, Germany
[13]Department of General and Thoracic Surgery University Hospital Giessen, Giessen, Germany
[14]Department of Pathology, Justus Liebig University, Giessen, Germany
[15]Department of Laboratory Medicine, Medical University of Vienna, Vienna, Austria
[16]Institute of Molecular Oncology, Philipps-University, Marburg, Germany
[17]Department of Thoracic Oncology, Airway Research Center North, DZL, Lungen Clinic, Grosshansdorf, Germany
[18]Department for Immunity of Inflammation, Mannheim Institute for Innate Immunoscience (MI3), Medical Faculty Mannheim, Heidelberg University, Mannheim, Germany
[19]Department of Medicine, Quebec Heart and Lung Institute, Laval University, Quebec, QC, Canada
[20]Lead contact
*Correspondence: savai.rajkumar@innere.med.uni-gieesen.de
https://doi.org/10.1016/j.cmet.2026.05.005

SUMMARY

Tumor-associated macrophages (TAMs) possess both tumor-promoting and tumor-inhibiting roles. Here, we explore TAMs' anti-tumor functions, focusing on the immune responsive gene 1 (IRG1) and its product, itaconate, in lung cancer development. Spatial metabolomics reveals that endogenous itaconate is markedly depleted within lung tumor regions compared with adjacent non-tumor tissue. Single-cell RNA sequencing shows that macrophages are the primary cells expressing IRG1 in human and mouse lung tumors. Both IRG1 knockout and transplantation of IRG1-depleted bone marrow leads to increased lung tumor growth in various mouse lung tumor models. Additionally, 4-octyl itaconate (Octyl Ita) reduces tumor growth *in vitro*, *in vivo*, and in *ex vivo* human tumor precision-cut lung slices. An integrated multi-omics analysis shows that IRG1/itaconate causes a metabolic shift in cancer cell and pro-tumor macrophages, mainly by inhibiting the pentose phosphate pathway (PPP) through targeting glucose-6-phosphate dehydrogenase (G6PD) activity, thereby suppressing cancer cell growth and transforming pro-tumor macrophages into anti-tumor macrophages. Thus, leveraging IRG1/itaconate's tumor-suppressive effects or using Octyl Ita could be a novel lung cancer therapy.

INTRODUCTION

Lung cancer is the most frequently diagnosed malignant disease worldwide and is associated with the highest mortality rate.[1] In recent decades, lung cancer mortality has declined due to reduced smoking, improved detection, and the emergence of immunotherapy. Unlike cytotoxic chemotherapy, immunotherapy targets the immune system rather than cancer cells,

 © 2026 The Author(s). Published by Elsevier Inc.
This is an open access article under the CC BY license (http://creativecommons.org/licenses/by/4.0/).

which represents a paradigm shift in treatment.[2,3] This paradigm shift reflects the modern view that cancer cells are not the only key players in tumors; immune and stromal cells within the tumor microenvironment (TME) also play a central role in lung tumor growth and metastasis.[4]

Among the immune cells in the TME of the lung, tumor-associated macrophages (TAMs) take center stage. These plastic cells exhibit a spectrum of phenotypes and functions that are determined by different TME signals. TAMs can be classified as ''yin and yang'' entities, with anti-tumor macrophages exhibiting an immune-activating and pro-inflammatory phenotype, while pro-tumor macrophages show an anti-inflammatory and angiogenic profile.[5,6] In lung cancer patients, the higher infiltration of anti-tumor macrophages and a lower presence of pro-tumor macrophages correlate with better survival.[7] We have shown that the proximity of pro-tumor macrophages to lung tumor cells contributes to tumor cell survival and poor prognosis in lung cancer patients.[6] Recent studies, including our own, have highlighted the plasticity of TAMs and demonstrated the potential for reprogramming of pro-tumor or anti-inflammatory macrophages to anti-tumor or pro-inflammatory macrophages through transcriptional and epigenetic changes.[8–11] However, the underlying mechanisms of macrophages' tumor-suppressive functions, the mechanistic distinction between pro- and anti-tumor macrophages, and the mechanisms that lead to the conversion of pro-tumor macrophages into anti-tumor macrophages are not yet well understood.

Metabolic divergence is a key difference between pro- and anti-inflammatory macrophages.[12] Despite the complexity of the TME in terms of nutrient and oxygen availability as crucial factors for cell metabolism, a simplistic view suggests that anti-tumor macrophages are heavily reliant on glycolysis compared with pro-tumor macrophages and have an impaired tricarboxylic acid (TCA) cycle, which leads to the accumulation of itaconate and succinate.

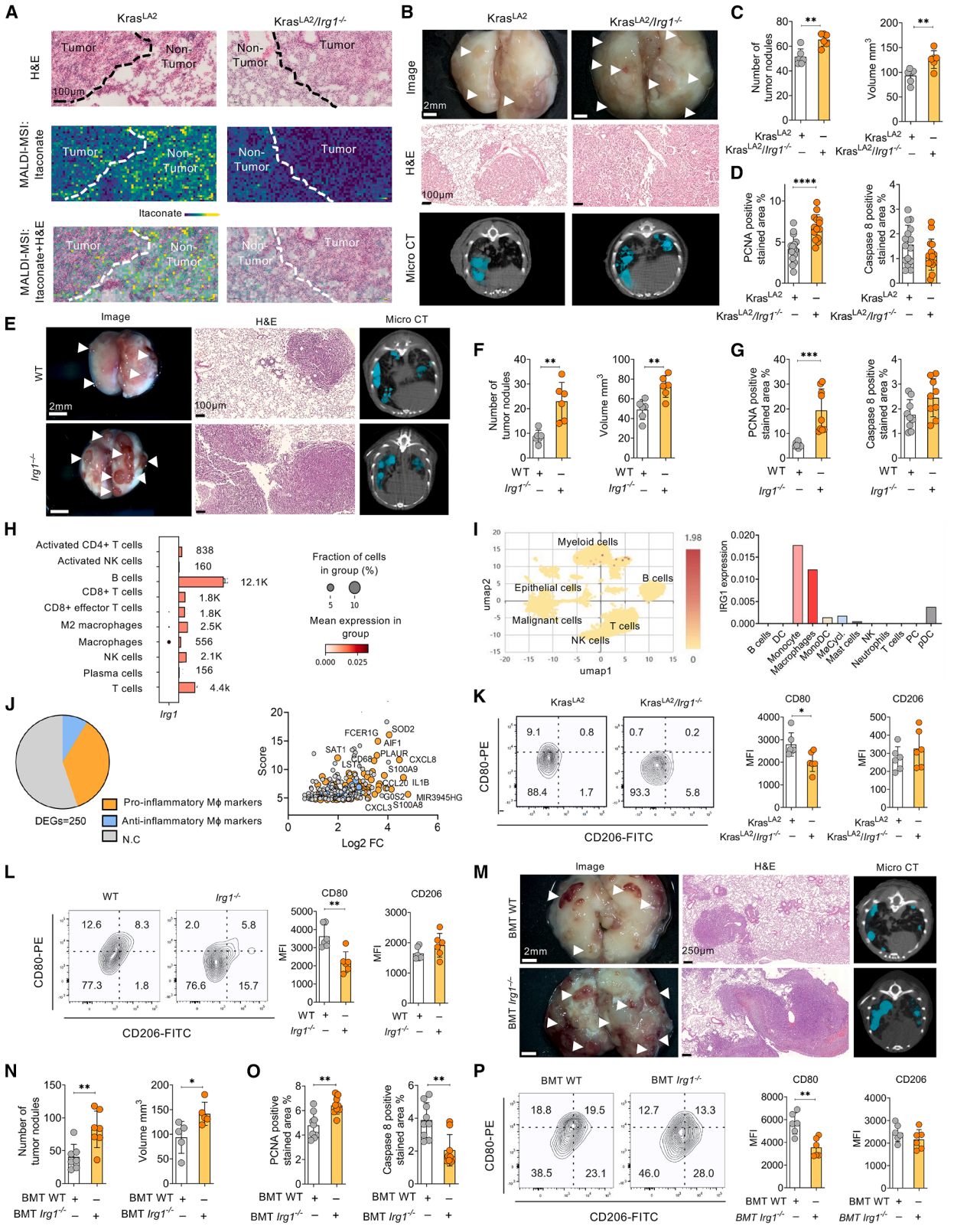
Itaconate is one of the most abundant metabolites produced intracellularly and extracellularly by macrophages after induction of the enzyme aconitate decarboxylase 1 (ACOD1/IRG1) by lipopolysaccharide (LPS), viral components, or interferon-gamma (IFN-γ).[13–17] IRG1/itaconate and its derivatives, which have been extensively studied in the context of host defense and inflammation, exert immunomodulatory functions in macrophages by inhibiting succinate dehydrogenase (SDHA) and glyceraldehyde-3-phosphate dehydrogenase (GAPDH), thus activating nuclear factor erythroid 2-related factor 2 (NRF2) and activating transcription factor 3 (ATF3), which epigenetically represses the TET-family DNA dioxygenase.[15,18–20] Compared with pro-inflammatory macrophages, the expression of IRG1/itaconate in anti-inflammatory macrophages is suppressed by several mechanisms, including the nuclear receptor peroxisome proliferator-activated receptor γ (PPARγ) and the microRNA miR-93/IRF9 axis, which highlights the inhibitory role of IRG1/itaconate in anti-inflammatory macrophage polarization.[21,22] In particular, the supplementation of anti-inflammatory macrophages with itaconate or 4-octyl itaconate (Octyl Ita), which is a penetrable itaconate derivative that targets Janus kinase-signal transducer and activator of transcription (JAK1/STAT6) signaling to suppress anti-inflammatory macrophage polarization.[23] Although the anti-inflammatory mechanisms in macrophages such as IRG1/itaconate do not necessarily imply that they are sufficient to promote tumor growth, we hypothesize that IRG1/itaconate may regulate various pro-tumorigenic functions beyond immunomodulation and thus play a crucial role in lung tumorigenesis. Spatial metabolomics revealed that endogenous itaconate is restricted to non-tumor lung regions, with minimal presence within tumor tissue. IRG1/itaconate deficiency accelerates lung tumor growth in various mouse models. In addition, we demonstrate that IRG1/itaconate is required for the anti-tumor macrophage phenotype, but it also directly alters lung cancer cell proliferation. Mechanistically, we elucidate IRG1/itaconate and Octyl Ita as novel inhibitors of G6PD activity that restrict cancer cell proliferation while orchestrating immunomodulatory effects in macrophages during lung tumorigenesis.

RESULTS

IRG1 ablation boosts lung tumor growth and metastasis

To assess endogenous itaconate during lung tumor development, we performed matrix-assisted laser desorption/ionization-mass spectrometry imaging (MALDI-MSI) on lung sections from $Kras^{LA2}$ and $Kras^{LA2}$/$Irg1^{-/-}$ mice. Itaconate was markedly reduced in tumor regions compared with adjacent non-tumor tissue, which indicated suppressed itaconate metabolism in lung tumors (Figure 1A). Itaconate was undetectable in $Kras^{LA2}$/$Irg1^{-/-}$ lungs, thus confirming its specificity and IRG1 dependence (Figure S1A). Using $Kras^{LA2}$/$Irg1^{-/-}$ and orthotopic $Irg1^{-/-}$ LLC1 models, we found that the *Irg1* loss significantly increased tumor growth and metastasis, with an increased tumor burden and proliferation but no change in apoptosis (Figures 1B–1G and S1B). Single-cell RNA sequencing (scRNA-seq) identified macrophages as the major *Irg1*-expressing population in the mouse lung TME[24] (Figure 1H). Consistently, two scRNA-seq datasets from human lung tumors showed that IRG1 expression was enriched in myeloid cells, particularly in macrophages and monocytes[25,26] (Figures 1I and S1C), with higher *Irg1* levels in normal lung tissue compared with tumors (Figure S1D). *Irg1* expression was also higher in $CD68^+$ macrophages from normal human lungs than in TAMs (Figure S1E). $IRG1^+$ TAMs exhibited a pro-inflammatory, anti-tumor transcriptional program[8,27] (Figure 1J), whereas TAMs from $Irg1^{-/-}$ tumors showed a pro-tumor phenotype, with reduced CD80 and increased CD206 (Figures 1K, 1L, and S1F).

Bone marrow transplantation demonstrated that hematopoietic IRG1 deficiency was sufficient to accelerate LLC1 tumor progression, thus increasing proliferation, reducing apoptosis, and decreasing CD80 expression in TAMs (Figures 1M–1P and S1G). Consistently, $Irg1^{-/-}$ bone marrow-derived macrophages (BMDMs) exhibited upregulation of *arginase1* (*Arg1*) and *found in inflammatory zone 1* (*Fizz1*) and downregulation of *tumor necrosis factor* (*Tnf*), and their conditioned media (CM) promoted tumor cell proliferation while reducing apoptosis (Figure S1H and S1I). Immune profiling revealed macrophages as the only immune population that was consistently altered across models, with minor context-dependent changes in natural killer (NK) cells and $CD8^+$ T cells (Figure S1J). Olink proteomics further revealed a pro-tumor soluble signature in *Irg1*-deficient tumors, which included increased chemokines and growth factors (C-X-C motif chemokine ligand 1 [Cxcl1], C-C motif chemokine ligand 3 [Ccl3],



(legend on next page)

platelet-derived growth factor subunit B [Pdgfb], and aryl hydrocarbon receptor [Ahr]) and reduced factors linked to anti-tumor immunity and tissue repair (lipoprotein lipase [Lpl], C-C motif chemokine ligand 20 [Ccl20], and transforming growth factor alpha [Tgfa]) (Figure S1K). Collectively, these data show that IRG1 and itaconate restrict lung tumor growth and metastasis by regulating macrophage programming in the lung TME.

Octyl Ita inhibits lung tumor growth *in vivo*, *ex vivo*, and *in vitro*

To evaluate the therapeutic potential of IRG1-derived itaconate, we examined the cell-permeable derivative Octyl Ita in *in vivo*, *ex vivo*, and *in vitro* lung cancer models. In $Kras^{LA2}$ mice treated from 4 to 12 weeks of age, MALDI-MSI confirmed the presence of increased lung itaconate levels following Octyl Ita administration (Figures 2A and S2A). Octyl Ita significantly suppressed tumor progression and reduced both total tumor area and lesion size (Figures 2B and 2C). In an orthotopic LLC1 model, Octyl Ita similarly reduced lung tumor burden and metastasis, with fewer and smaller tumor nodules and decreased proliferation without changes in apoptosis (Figures 2D, S2B, and S2C). TAMs shifted toward an anti-tumor phenotype, with reduced CD206 and preserved CD80 expression upon Octyl Ita treatment (Figure S2D). Comparable effects were observed in subcutaneous LLC1 tumors, where Octyl Ita reduced tumor growth, decreased proliferation, increased apoptosis, and lowered CD206 expression without affecting CD80 (Figures S2E–S2G). Other immune populations were largely unchanged, except for the increased $CD8^+$ T cells in the subcutaneous model (Figures S2H and S2I).

To assess translational relevance, tumor-derived precision-cut lung slices (TD-PCLSs) from human lung cancer specimens were treated with Octyl Ita. Treatment increased itaconate levels in TD-PCLSs and significantly reduced cellular proliferation without affecting apoptosis, while selectively enriching anti-tumor TAMs ($CD80^+$), with pro-tumor TAMs ($CD206^+$) and other immune populations remaining unchanged (Figures 2E–2G and S3A–S3C). We next assessed tumor-cell-intrinsic effects. At a viability-guided dose (250 μM; Figure S3D), Octyl Ita potently inhibited proliferation across lung cancer cell lines regardless of Kelch-like ECH-associated protein 1 (KEAP1) status, which indicated KEAP1/NRF2-independent activity (Figure 2H). In A549 cells, Octyl Ita reduced cell numbers with a modest increase in apoptosis and rapidly increased intracellular itaconate levels (Figures 2I–2K). Exogenous itaconate also suppressed proliferation but required higher concentrations and was less effective than Octyl Ita (Figures 2L and S3E). Consistently, IRG1 overexpression reduced proliferation and cell numbers without affecting apoptosis in A549 and KEAP1-deficient H1650 cells (Figures S3F–S3H). Together, these data establish IRG1/itaconate as a potent inhibitor of lung tumor growth by directly restraining tumor cell proliferation and promoting anti-tumor macrophage states.

Octyl Ita suppresses the pentose phosphate pathway and disrupts antioxidant signaling

To assess whether Octyl Ita-mediated growth suppression via metabolic rewiring, we profiled its metabolic influences in A549 cells. Liquid chromatography-mass spectrometry (LC-MS) revealed the rapid depletion of pentose phosphate pathway (PPP) intermediates within 6 h of treatment, which intensified by 24 h (Figures 3A and 3B). A reduced ribose-5-phosphate (R5P)/ribulose-5-phosphate (Ru5P) ratio indicated impaired oxidative PPP activity (Figure 3C). Consistently, [1,2-$^{13}C_2$]-glucose tracing showed reduced M + 1 labeling of pentose phosphates (R5P, Ru5P, and xylose-5-phosphate [X5P]), which confirmed a decreased oxidative PPP flux (Figure 3D). The increased lactate M + 2/M + 1 ratio suggested reduced glucose shunting into the oxidative PPP rather than enhanced glycolysis (Figure 3E). Accordingly, M + 2 labeling increased in dihydroxyacetone (DHAP) and glyceraldehyde-3-phosphate (G3P) (Figures 3F and 3G), whereas M + 2 incorporation into sedoheptulose-7-phosphate (S7P) decreased, which indicated the

Figure 1. IRG1 regulates lung tumor growth and metastasis

(A) H&E staining, MALDI-MSI ion maps, and overlays showing itaconate localization in lung tumors from $Kras^{LA2}$ and $Kras^{LA2}$/*Irg1*$^{-/-}$ mice (n = 3 biological replicates for each genotype). The ion maps display the spatial distribution of itaconate, with signal intensity coded from low (blue) to middle (green) and high (yellow). Scale bars, 100 μm.

(B–D) (B) Representative gross lung images (2 mm), H&E sections (100 μm), and micro-computed tomography (CT) images, with the arrowheads indicating tumor nodules; (C) tumor nodule number and total lung tumor volume quantified by micro-CT (n = 6 biological replicates for each genotype); (D) quantification of PCNA and caspase-8 immunofluorescence in DAPI-defined tumor regions, normalized to tumor area (n = 15 technical replicates from 4 biological replicates for each genotype) from $Kras^{LA2}$ and $Kras^{LA2}$/*Irg1*$^{-/-}$ mice.

(E–G) (E) Representative lung images (2 mm), H&E sections (100 μm), and micro-CT images; (F) tumor nodule number and total lung tumor volume by micro-CT (n = 6 biological replicates for each genotype); (G) quantification of PCNA and caspase-8 immunofluorescence (n = 9 technical replicates from 3 biological replicates for each genotype) from WT and *Irg1*$^{-/-}$ mice injected intravenously with LLC1 cells.

(H) scRNA-seq of $CD45^+$ cells from mouse lung tumors showing *Irg1* expression across immune subsets; bar height indicates mean expression and circle size indicates expressing cell frequency.

(I) Uniform manifold approximation and projection (UMAP) of scRNA-seq from metastatic human lung adenocarcinoma showing enrichment of $IRG1^+$ cells in myeloid populations.[25,26]

(J) Top 250 differentially expressed genes (DEGs) between *IRG1*$^+$ and *IRG1*$^-$ macrophages categorized by pro-inflammatory and anti-inflammatory macrophage markers. N.C. = not categorized.

(K and L) CD80 and CD206 mean fluorescence intensity (MFI) in lung macrophage from $Kras^{LA2}$ and $Kras^{LA2}$/*Irg1*$^{-/-}$ and from WT and *Irg1*$^{-/-}$ mice injected with LLC1 cells (n = 6 biological replicates for each genotype).

(M) Representative lung images (2 mm), H&E sections (250 μm), and micro-CT images, with the arrowheads indicating the tumor nodules.

(N) Tumor nodule number (n = 7 biological replicates for each group) and total lung tumor volume by micro-CT (n = 5 biological replicates for each group).

(O) Quantification of PCNA and caspase-8 immunofluorescence (n = 9 technical replicates from 3 biological replicates for each group).

(P) CD80 and CD206 MFI in lung macrophages (n = 6 biological replicates for each group) from WT irradiated mice, reconstituted with WT or *Irg1*$^{-/-}$ bone marrow and injected with LLC1 cells.

Data are mean ± SEM. Statistical significance was determined by two-tailed unpaired Student's t test. *p < 0.05, **p < 0.01, ***p < 0.001, and ****p < 0.0001.

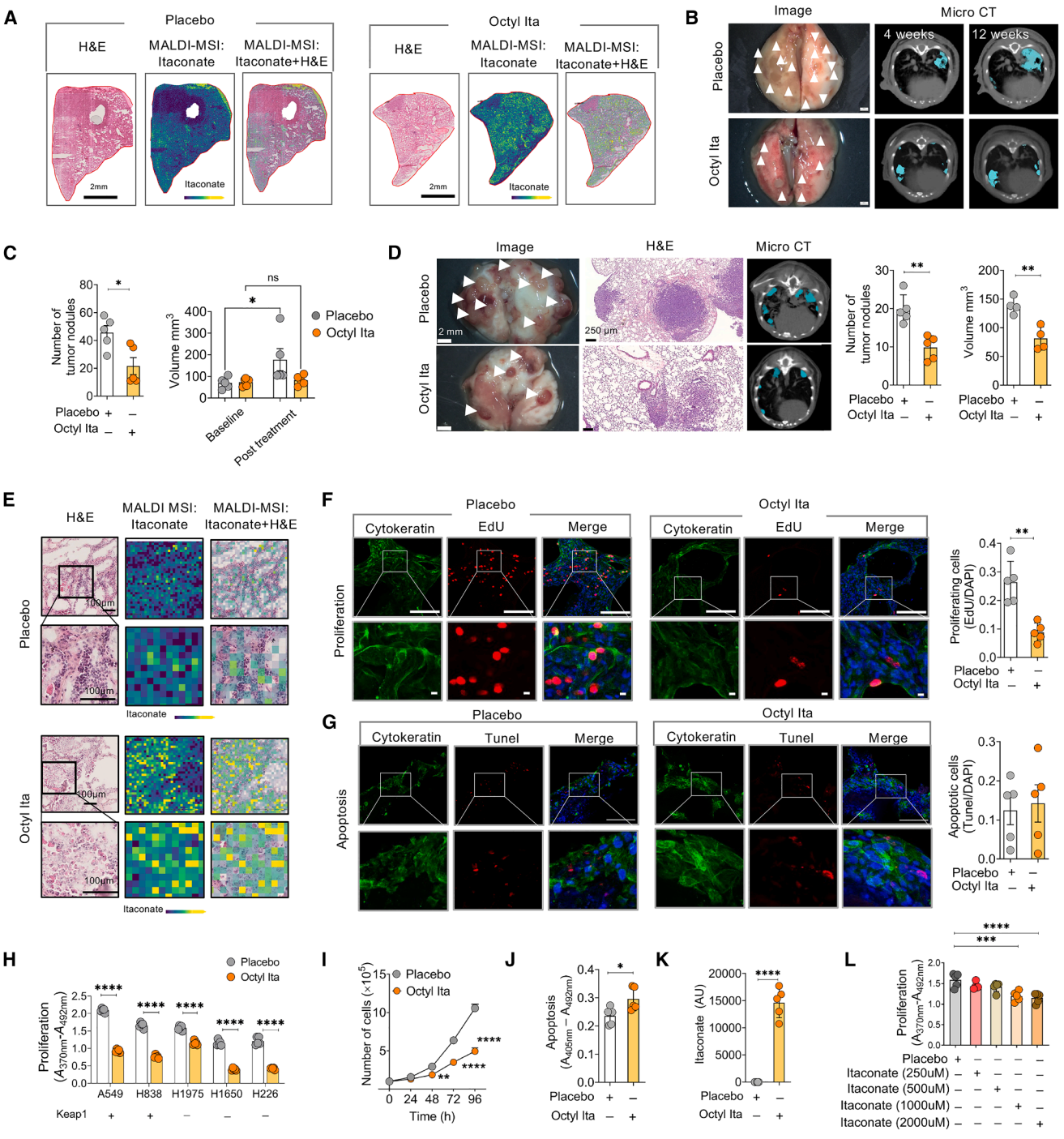


Figure 2. Octyl Ita inhibits the growth and metastasis of lung tumors both *in vivo* and *ex vivo* and *in vitro*

(A) MALDI-MSI ion maps and H&E overlays showing increased itaconate in lungs of Kras^{LA2} mice treated with placebo or Octyl Ita (100 mg/kg) for 8 weeks (n = 3 biological replicates for each group). The ion maps display the spatial distribution of itaconate, with signal intensity coded from low (blue) to middle (green) and high (yellow). Scale bar, 2 mm.

(B and C) Representative lung images and longitudinal micro-CT scans with quantification of tumor nodules and total lung tumor volume in placebo- and Octyl Ita-treated Kras^{LA2} mice; the arrowheads indicate the tumor nodules (n = 5 biological replicates for each group).

(D) Representative lung images, H&E sections, and micro-CT scans from LLC1-injected mice treated with Octyl Ita, with quantification of tumor nodules (n = 5 biological replicates for each group) and lung tumor volume (n = 4 biological replicates for each group). The arrowheads indicate the tumor nodules. Scale bar, 2 mm.

(legend continued on next page)

suppression of both oxidative and non-oxidative PPP branches (Figure 3H). Accordingly, Octyl Ita lowered glutathione (GSH) levels and reduced the GSH/GSSG ratio, which was consistent with impaired PPP-derived NADPH production (Figure 3I). These changes occurred without global alterations in glycolysis or mitochondrial respiration, as the oxygen consumption rate (OCR) and the extracellular acidity rate (ECAR) remained unchanged (Figure S4A). Together, these data support a model in which Octyl Ita inhibits PPP flux, which induces redox stress without broadly increasing glycolysis.

To assess PPP activity *in vivo*, MALDI-MSI of $Kras^{LA2}$ lung tumors revealed distinct metabolic segmentation, with tumor regions enriched for D-ribose-5-phosphate and GSH, whereas endogenous itaconate localized predominantly to adjacent non-tumor tissue (Figures 3J, 3K, and S4B). These spatial patterns suggest the metabolic exclusion of intrinsic itaconate from PPP-active tumor regions. To define downstream programs, we performed transcriptomic and proteomic profiling of A549 cells after 48-h Octyl Ita treatment. Transcriptomics showed the induction of stress-response pathways, which included xenobiotic/heme metabolism and TNF/nuclear factor kappa-light-chain-enhancer of activated B cells (NF-κB) signaling, alongside alterations in glycolysis and lipid metabolism (Figures 3L and S4C). Proteomics revealed a broad suppression of proliferation-associated programs, which included E2F targets, the G2/M checkpoint, MYC signaling, the mitotic spindle, and the mechanistic target of rapamycin complex 1 (mTORC1) pathways (Figures 3M and S4D). Integrative network analysis grouped regulated pathways into functional communities, which revealed a coordinated downregulation of cell cycle and proliferation modules (C1-C2) at both RNA and protein levels, alongside prominent alterations in stress- and redox-associated pathways including reactive oxygen species (ROS) responses, peroxisomal pathways, phosphatidylinositol 3-kinase (PI3K)-AKT-mTOR, UV response, and TNF signaling (C9-C6) (Figures 3N and S4E). Among the most induced features, heme oxygenase 1 (HMOX1) was strongly upregulated at both the transcript and protein levels (Figure S4F), which is consistent with oxidative stress that is triggered by PPP inhibition and glutathione depletion. Collectively, these data identify PPP suppression as a primary metabolic consequence of Octyl Ita treatment, which leads to a redox imbalance and a coordinated repression of proliferative signaling programs.

Octyl Ita inhibits G6PD activity and drives anti-proliferative effects

We first tested whether Octyl Ita alters PPP regulation through NRF2. Neither NRF2 protein levels nor expression of PPP enzymes (G6PD, 6-phosphogluconate dehydrogenase [PGDH], transaldolase 1 (TALDO), and transketolase [TKT]) changed after 6-h treatment (Figures 4A and S4G). Given the rapid suppression of PPP flux, we focused on G6PD as a potential target. Octyl Ita significantly reduced G6PD activity in A549 cells without affecting protein abundance (Figures 4A and 4B). IRG1 overexpression similarly decreased G6PD activity without altering NRF2 or G6PD expression (Figure S4H). Kinetic analyses showed a reduced G6PD V_{max} (1.52 → 1.19 U) with a minimal change in K_m (188 → 178 μM), which indicated impaired catalytic efficiency (Figure 4C). Recombinant G6PD exhibited the same inhibition pattern following itaconate treatment, with a reduction in V_{max} (2.83 → 1.55 U) and only slight K_m changes (Figures 4D and 4E).

Molecular docking predicted that both Octyl Ita and itaconate bind to G6PD, with Octyl Ita showing a slightly higher affinity (−5.9 vs. −5.2 kcal/mol), which is consistent with greater enzymatic inhibition (Figures 4F, 4G, and S4I). ITalk chemoproteomic enrichment followed by liquid chromatography-tandem mass spectrometry (LC-MS/MS) detected no G6PD enrichment or cysteine modification after 6-h treatment, which confirmed that neither Octyl Ita nor itaconate covalently modified G6PD (Figure S4J). Together with recombinant assays, this demonstrates that Octyl Ita inhibits G6PD through non-covalent pocket binding.

To test whether G6PD inhibition underlies the anti-proliferative effect of Octyl Ita, we examined its impact on G6PD-deficient cells and observed that Octyl Ita failed to further reduce proliferation in G6PD-knockdown A549 cells (Figures 4H and S4K). Supplementation with downstream PPP metabolites (6-phosphogluconate [6GP], D-ribose [DR], and ribose-5-phosphate [R5P]) dose-dependently rescued proliferation, whereas antioxidant treatment with N-acetylcysteine (NAC) had no effect (Figures 4I and 4J). G6PD knockdown phenocopied Octyl Ita-induced growth inhibition and was similarly rescued by PPP metabolites (6GP, DR, and R5P) (Figure S4L). Overexpression of TKT to increase non-oxidative PPP flux partially restored proliferation (Figure S4M), which indicated that reduced ribose production rather than NADPH depletion is the primary driver of growth suppression. We next examined stress signaling downstream of G6PD inhibition. G6PD-deficient cells displayed elevated basal HMOX1 levels, which were reduced by NAC, thus indicating ROS dependence (Figure S4N). Octyl Ita-induced HMOX1 expression was similarly NAC sensitive (Figure S4O). Importantly, Octyl Ita did not further increase HMOX1 or ROS levels in G6PD-deficient cells (Figures 4K and 4L). Together, these data demonstrate that

(E) MALDI-MSI ion maps and H&E overlays from tumor-derived precision-cut lung slices (TD-PCLS) treated with DMSO or Octyl Ita (250 μM) for 24 h (n = 3 biological replicates for each group). The ion maps display the spatial distribution of itaconate, with signal intensity coded from low (blue) to middle (green) and high (yellow). Scale bars, 100 μm.
(F and G) Representative images and quantification of proliferation (EdU) and apoptosis (TUNEL) in TD-PCLS after 48-h treatment (n = 5 biological replicates for each group). The tumor regions are identified by cytokeratin staining. Scale bars, 250 μm (overview) and 50 μm (zoom).
(H) Proliferation of lung cancer cell lines treated with Octyl Ita for 48 h (n = 5 biological replicates for each group).
(I) A549 cell counts after 96-h treatment with Octyl Ita (250 μM) (n = 3 biological replicates for each group).
(J) Apoptosis of A549 cells after 48-h treatment with Octyl Ita (250 μM) (n = 5 biological replicates for each group).
(K) Intracellular itaconate levels in A549 cells after 6-h Octyl Ita treatment (n = 5 biological replicates for each group).
(L) Proliferation of A549 cells after 48-h treatment with itaconate (250–2,000 μM; pH 7.5) (n = 5 biological replicates for each group).
Data are mean ± SEM. Statistical significance was determined by two-tailed unpaired Student's t test or one- and two-way ANOVA. *$p < 0.05$, **$p < 0.01$, ***$p < 0.001$, and ****$p < 0.0001$.

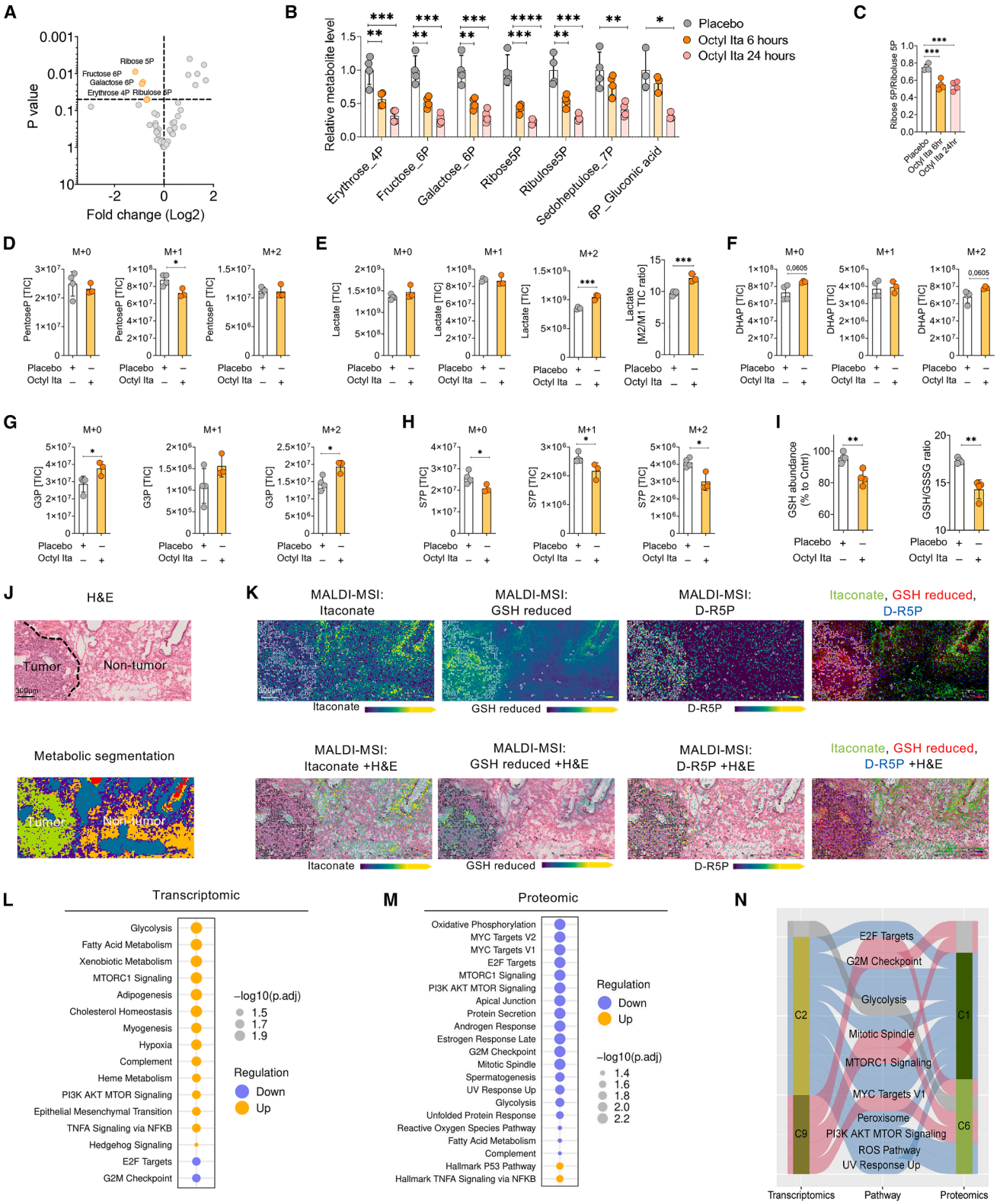


Figure 3. Octyl Ita regulates PPP and associated signaling pathways in lung cancer cells

(A) Volcano plot showing that PPP metabolites are decreased in A549 cells after 6-h treatment with Octyl Ita (250 μM) (n = 2–4 biological replicates for each group).
(B) LC-MS quantification of PPP metabolites after 6- and 24-h treatment, normalized to placebo in A549 cells (n = 3–4 biological replicates for each group).
(C) R5P/Ru5P ratio after 6- and 24-h treatment in A549 cells (n = 4 biological replicates for each group).

(legend continued on next page)

Octyl Ita suppresses cancer cell proliferation primarily through non-covalent inhibition of G6PD, which limits PPP-derived ribose production and activates a G6PD-ROS-HMOX1 stress-response pathway.

IRG1/itaconate regulation of G6PD activity in macrophages and induction of an anti-tumor phenotype

To determine whether Octyl Ita modulates macrophage function in the TME, we analyzed TAMs from human lung tumors. Freshly isolated TAMs expressed low IRG1 (Figure S1E), but *ex vivo* treatment with Octyl Ita for 24 h increased *TNF* and *CD80* expression while reducing colony stimulating factor 1 receptor (*CSF1R*) and *CD206*, which indicated a shift toward a more pro-inflammatory phenotype (Figures S5A and S5B). CM from Octyl Ita-treated TAMs suppressed A549 proliferation relative to control CM (Figure S5C), which demonstrated functional consequences for tumor-macrophage crosstalk.

To define the metabolic basis of this effect, we examined peripheral blood mononuclear cell (PBMC)-derived human macrophages across defined polarization states. LPS/IFNγ-stimulated pro-inflammatory macrophages exhibited high IRG1 expression and itaconate production, reduced G6PD activity, and CM that suppressed tumor cell proliferation and promoted apoptosis. In contrast, interleukin-4 (IL-4)-stimulated anti-inflammatory macrophages displayed lower IRG1/itaconate levels, elevated G6PD activity, and a tumor-supportive CM (Figures 5A, 5B, S5D, and S5E). Octyl Ita reprogrammed anti-inflammatory macrophages toward a tumor-suppressive state, as CM from treated cells reduced A549 proliferation more effectively than direct Octyl Ita exposure, without significantly affecting apoptosis (Figures 5C and S5F). Metabolically, Octyl Ita suppressed PPP intermediates, reduced the R5P/Ru5P ratio, and decreased G6PD activity without altering protein abundance in anti-inflammatory macrophages (Figures 5D, 5E, and S5G–S5I).

Transcriptomic and proteomic remodeling of anti-inflammatory macrophages by Octyl Ita

To define the transcriptional consequences of PPP suppression, we profiled anti-inflammatory macrophages treated with Octyl Ita or DMSO and compared them with pro-inflammatory macrophages. Principal-component analysis of transcriptomic data showed that Octyl Ita shifted anti-inflammatory macrophages away from their baseline state (Figure 5F). Pathway analysis confirmed that pro-inflammatory macrophages were enriched for inflammatory and stress-associated programs, which included TNF/NF-κB, IFN signaling, IL-6/JAK-STAT, p53, and apoptosis (Figure 5G, left). Octyl Ita-induced overlapping stress pathways in anti-inflammatory macrophages, which included p53 signaling, ROS response, xenobiotic metabolism, and unfolded protein response, while increasing pro-inflammatory markers and suppressing anti-inflammatory markers (Figures 5G, middle, and S5J). However, IFN-driven signatures were not fully restored, which indicated that there was only partial convergence toward the pro-inflammatory state (Figure 5G, right). Consistent with stress activation, Octyl Ita increased NRF2 protein levels in anti-inflammatory macrophages (Figure S5K). Proteomics confirmed a strong activation of stress-adaptive pathways, which included glycolysis, hypoxia, mTORC1, and ROS signaling, with HMOX1 among the most induced proteins (Figures 5H and 5I). Multi-omics network analysis identified two coordinated modules: a stress-response cluster (C1) that was upregulated at both RNA and protein levels, and a metabolic rebalancing cluster (C18) that involved fatty acid metabolism, peroxisome function, and cholesterol homeostasis (Figures 5J and S5L). Transcriptomic communities linked to xenobiotic metabolism, glycolysis, and TNF/NF-κB signaling (C20, C9) were tightly connected to these proteomic modules, which indicated integrated stress and metabolic rewiring (Figure 5J). Collectively, these data show that Octyl Ita reprograms anti-inflammatory macrophages toward a stress-activated, partially pro-inflammatory state that is associated with redox signaling and metabolic remodeling.

Functional consequences: PPP output and G6PD status shape macrophage-tumor interactions

Functionally, the supplementation of CM from Octyl Ita-treated anti-inflammatory macrophages with PPP metabolites partially rescued tumor cell proliferation, which indicated that reduced PPP output limits macrophages' tumor-supportive capacity (Figure 5K). We next tested whether tumor cell G6PD influences sensitivity to macrophage-derived signals. CM from Octyl Ita-treated anti-inflammatory macrophages suppressed the proliferation of G6PD-deficient tumor cells less effectively than control cells (Figure S5M), which suggests a partial dependence on tumor cell G6PD. Furthermore, silencing G6PD in anti-inflammatory macrophages promoted a more inflammatory phenotype (increasing *TNF* and *CD80* without significantly affecting *CSF1R* and *CD206*) and constrained Octyl Ita-mediated reprogramming, which resulted in higher tumor cell proliferation compared with control macrophage CM (Figures 5L and 5M). Apoptosis was unchanged across CM conditions (Figure S5N). Notably, HMOX1 induction in macrophages occurred largely

(D–H) [$^{1,2}13C_2$] glucose tracing in A549 cells pretreated with Octyl Ita or DMSO for 6 h, followed by 30-min labeling in the continued presence of Octyl Ita. Isotopologue distributions of (D) pentose phosphates (R5P/Ru5P/X5P), (E) lactate, (F) dihydroxyacetone phosphate, (G) glyceraldehyde-3-phosphate, and (H) sedoheptulose-7-phosphate were quantified by LC-MS (n = 4 placebo, n = 3 Octyl Ita biological replicates for each group).

(I) Glutathione (GSH) levels and GSH/GSSG ratio after 6-h Octyl Ita treatment (Cntrl = control) (n = 4 biological replicates for each group).

(J) H&E staining and MALDI-MSI-based metabolic segmentation of $Kras^{LA2}$ lung tumors identifying distinct tumor and non-tumor metabolic regions.

(K) MALDI-MSI ion images showing spatial distribution of itaconate, GSH, and D-ribose-5-phosphate within the same tumor section with signal intensity coded from low (blue) to middle (green) and high (yellow). Scale bar, 300 μm.

(L and M) Pathway enrichment analysis of transcriptomic and proteomic changes in A549 cells after 48-h Octyl Ita treatment (n = 4 biological replicates for each group).

(N) Sankey plot summarizing significantly enriched pathways (adjusted $p < 0.05$) across functionally related transcriptomic and proteomic communities.

Data are mean ± SEM. Statistical significance was determined by two-tailed unpaired Student's t test or one-way ANOVA. *$p < 0.05$, **$p < 0.01$, ***$p < 0.001$, and ****$p < 0.0001$.

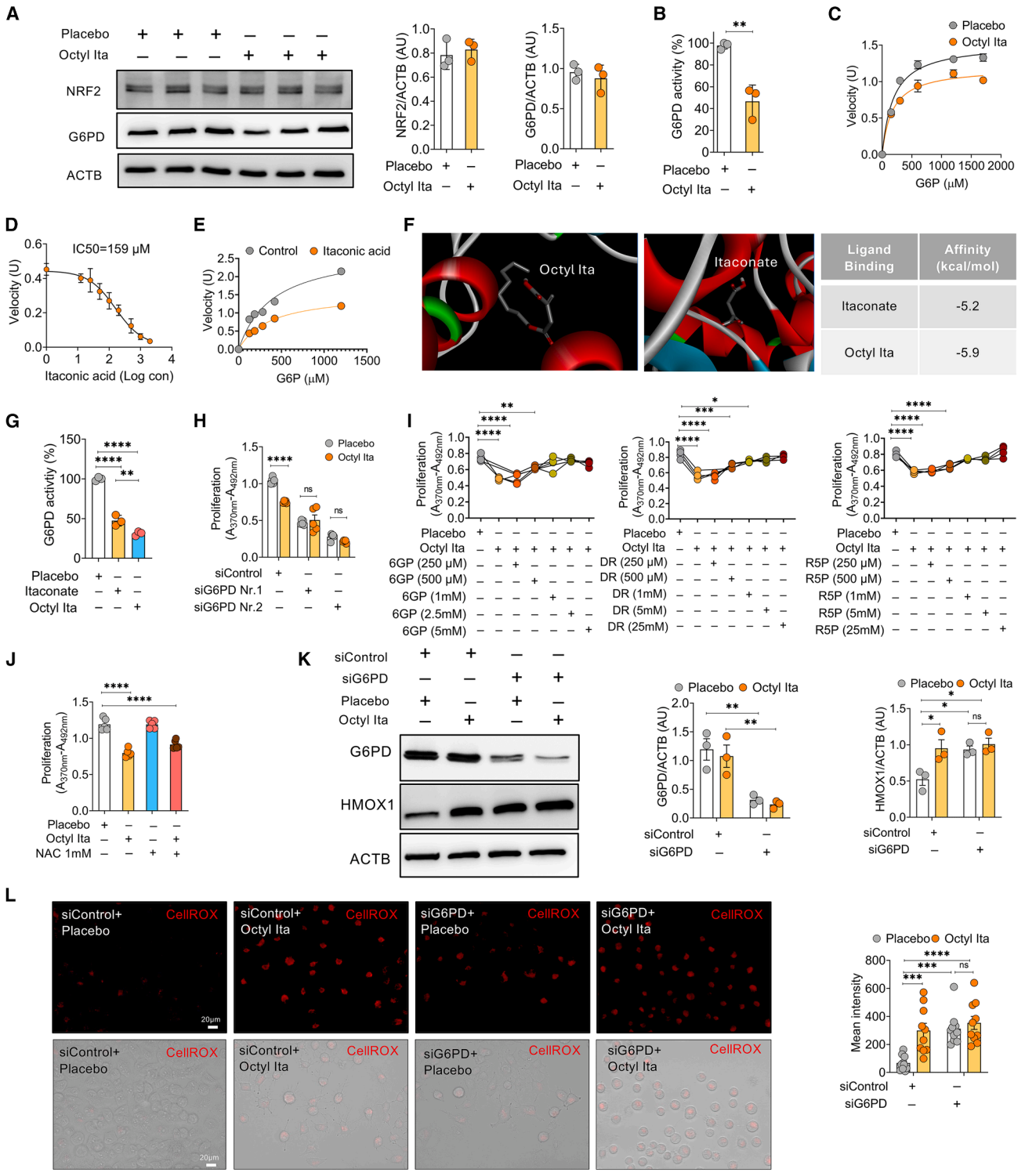


Figure 4. Octyl Ita targets G6PD and inhibits proliferation

(A) Immunoblot analysis and quantification of NRF2 and G6PD in A549 cells after 6-h Octyl Ita treatment; ACTB, loading control (n = 3 biological replicates for each group).

(B) G6PD activity measured by NADPH production in A549 cells after 6-h Octyl Ita treatment (n = 3 biological replicates for each group).

(C) Michaelis-Menten kinetics of G6PD activity in A549 cell homogenates (mean of three independent experiments).

(D) Activity of recombinant human G6PD following incubation with increasing concentrations of itaconate (n = 3 independent experiments for each group).

(E) Michaelis-Menten kinetics of recombinant G6PD activity in the presence or absence of itaconate (mean of three independent experiments).

(legend continued on next page)

independently of G6PD status, which distinguished macrophage stress responses from those in tumor cells (Figure S5O).

The endogenous IRG1/itaconate pathway regulates G6PD and macrophage phenotype

Given these findings, we tested whether endogenous IRG1/itaconate similarly regulates macrophage metabolism. IRG1 knockdown in pro-inflammatory macrophages at 6 h, when IRG1 and secreted itaconate were increased (Figure S6A and S6B), led to G6PD activity enhancement without altering protein abundance and reduced itaconate production (Figures S6C–S6E). Consistently, *Irg1*$^{-/-}$ mouse BMDMs displayed elevated G6PD activity following LPS stimulation, and increased G6PD activity was also observed in macrophages isolated from *Irg1*$^{-/-}$ → wild-type (WT) bone marrow chimeras bearing LLC1 tumors (Figure S6F), which confirmed conserved metabolic regulation. IRG1-deficient pro-inflammatory macrophages adopted a pro-tumor phenotype, with reduced *TNF* and *CD80*, increased *CSF1R* and *CD206*, and CM that promoted tumor cell proliferation (Figures S6G and S6H). To test whether G6PD mediates this phenotype, we silenced G6PD during pro-inflammatory polarization. G6PD knockdown partially restored anti-tumor features by increasing *TNF* and *CD80*, reducing *CSF1R* and *CD206*, and suppressing tumor cell proliferation without altering apoptosis (Figures S6I and S6J). Finally, since macrophages export itaconate via ATP-binding cassette subfamily G member 2 (ABCG2), we assessed the role of extracellular itaconate. ABCG2 knockdown attenuated the anti-proliferative activity of CM from pro-inflammatory macrophages (Figure S6K), which indicated that secreted itaconate contributes to macrophage-mediated tumor suppression. Together, these data establish an endogenous IRG1/itaconate-G6PD axis that regulates PPP activity and macrophage polarization, which limits tumor-supportive functions through both intracellular metabolic control and extracellular itaconate signaling.

Impact of IRG1 ablation and Octyl Ita treatment on *in vivo* G6PD activity in lung tumors

We next assessed whether IRG1 loss and Octyl Ita treatment modulate G6PD activity *in vivo*. Across multiple lung tumor models, IRG1-deficient mice showed significantly elevated *in situ* G6PD activity compared with WT controls (Figures 6A–6C), which is consistent with the reduced itaconate levels observed *in vitro*. In contrast, Octyl Ita treatment decreased G6PD activity in orthotopically implanted lung tumors relative to placebo-treated mice (Figure 6D), which mirrored its inhibitory effects in cultured cells. To determine whether this regulatory axis operates in human lung cancer, we examined G6PD activity in TAMs from lung cancer patient tumors. CD68^{+}/IRG1^{+} macrophages exhibited lower G6PD activity than CD68^{+}/IRG1^{-} macrophages (Figure 6E), which confirmed that endogenous IRG1/itaconate suppresses G6PD within the TME. Supporting the pro-tumor function of G6PD, human lung adenocarcinomas showed elevated G6PD activity (Figure 6F).

Clinically, high G6PD expression is correlated with significantly worse overall survival, whereas high ABCG2 expression—the itaconate exporter—was associated with improved outcomes (Figure 6G). This beneficial association of ABCG2 was strongest in stage I tumors, which suggested that efficient itaconate export is particularly protective early in tumor development (Figure S6L). Notably, *ABCG2* mRNA was markedly reduced in human TAMs that had been isolated from lung tumors (Figure S6M), which indicated impaired itaconate turnover and export within the lung TME. Broader analyses across cancer types revealed a context-dependent role for itaconate. ABCG2 showed favorable prognostic associations (hazard ratio [HR] < 1) in lung and breast cancers, where itaconate has established anti-tumor functions (Figure S6N). In contrast, ABCG2 was correlated with poor prognosis (HR > 1) in colorectal and gastric cancers, which is consistent with reports that itaconate promotes tumor progression in these settings (Figure S6N). Together, these data demonstrate that the anti-tumor effects of the IRG1/itaconate axis in lung cancer are mediated through the suppression of G6PD and PPP activity. High G6PD levels are associated with aggressive tumor behavior and poor survival, whereas elevated ABCG2 reflects an enhanced itaconate export that is linked to a favorable prognosis. These findings support IRG1/itaconate-G6PD inhibition as a therapeutic strategy in lung cancer, where the metabolic and immune microenvironment enhances the anti-tumor actions of itaconate.

DISCUSSION

The key findings of this study strongly support a hitherto unknown anti-tumor effect of IRG1/itaconate in lung cancer (Figure 6H): (1) itaconate distribution was higher in non-tumor lung tissue than in tumor tissue together with acceleration of lung tumor development in IRG1-itaconate-depleted mice (Kras^{LA2}, orthotopic and bone marrow-transplanted models); (2) IRG1/itaconate critically shapes both macrophage and cancer cell behavior, as loss of IRG1 enhanced pro-tumor macrophage functions and increased cancer cell proliferation *in vivo*,

(F) Molecular docking of itaconate and Octyl Ita within the G6PD active site with predicted binding affinities.
(G) Recombinant G6PD activity following treatment with placebo, itaconate, or Octyl Ita (n = 3 independent experiments).
(H) Proliferation of A549 cells transfected with siG6PD or siControl, followed by Octyl Ita treatment (n = 5 biological replicates for each group).
(I) Rescue of A549 proliferation by pretreatment with PPP metabolites (6-phosphogluconate, D-ribose, and R5P) prior to Octyl Ita exposure (n = 4 biological replicates for each group).
(J) Effect of antioxidant pretreatment (N-acetyl cysteine) on Octyl Ita-mediated growth inhibition (n = 5 biological replicates for each group).
(K) Immunoblot analysis and quantification of HMOX1 and G6PD in siG6PD- and siControl-transfected A549 cells treated with Octyl Ita; ACTB, loading control (n = 3 biological replicates for each group).
(L) ROS levels measured by CellROX Orange fluorescence in siG6PD- and siControl-transfected A549 cells treated with Octyl Ita (n = 10 technical replicates from 3 biological replicates for each group). Scale bar, 20 μm
Data are mean ± SEM. Statistical significance was determined by two-tailed unpaired Student's t test or one- and two-way ANOVA. ns, not significant; $^{*}p < 0.05$, $^{**}p < 0.01$, $^{***}p < 0.001$, and $^{****}p < 0.0001$.

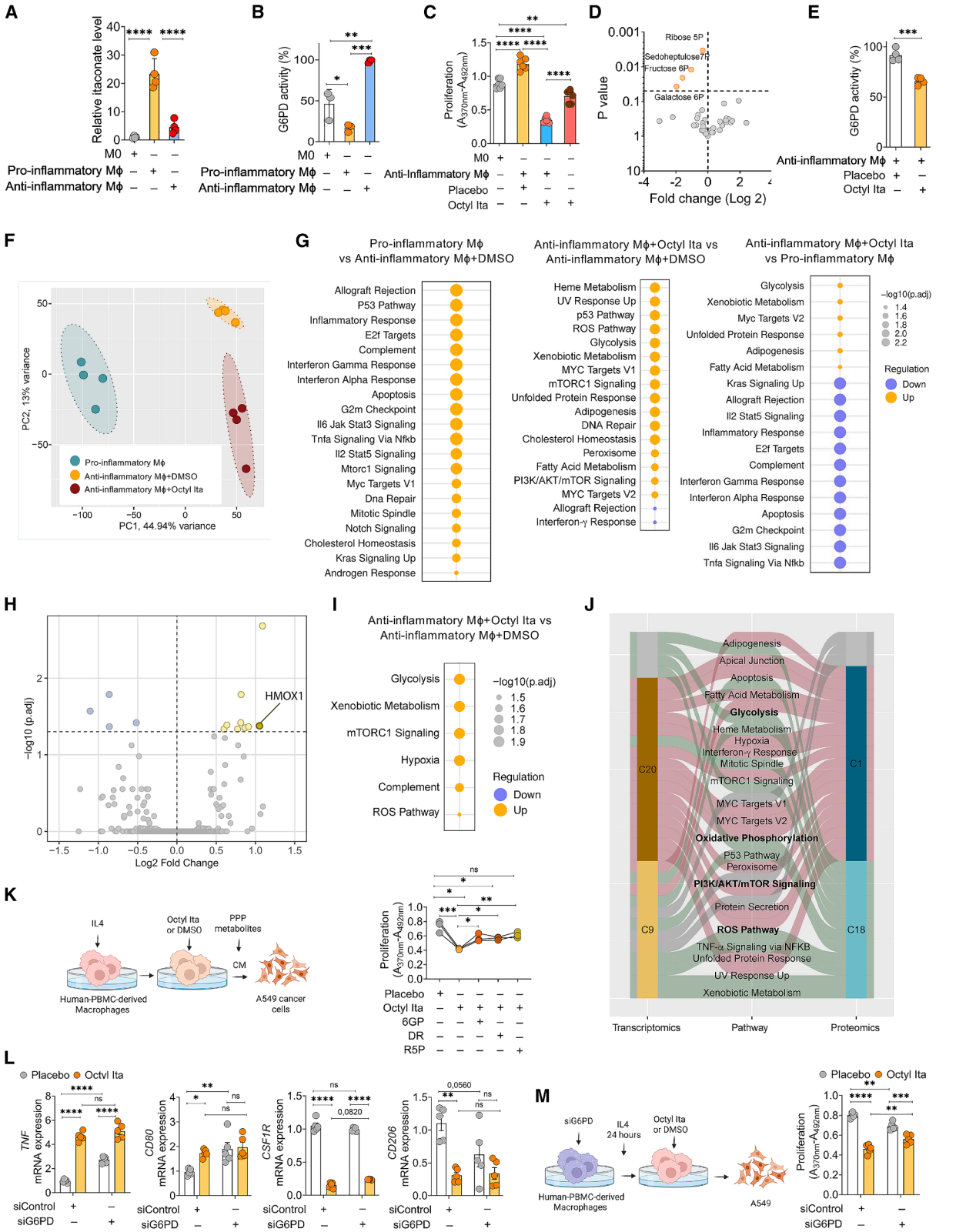


Figure 5. Octyl Ita modulates PPP and induces an anti-tumor phenotype in macrophages

(A) Intracellular itaconate levels measured in PBMC-derived human macrophages (M0), LPS/IFN-γ stimulated pro-inflammatory, and IL-4-stimulated anti-inflammatory macrophages (n = 4 biological replicates for each group).

(legend continued on next page)

while Octyl Ita both reprogrammed pro-tumor macrophages toward an anti-tumor phenotype and directly inhibited lung cancer cell proliferation *in vitro*, *ex vivo* (TD-PCLS), and *in vivo*; and (3) identification of IRG1/itaconate and Octyl Ita as inhibitors of PPP metabolism and G6PD activity that restrict cancer cell proliferation and introduce an anti-tumor phenotype in macrophages.

Spatial metabolomic imaging revealed that itaconate is enriched in non-tumor lung tissue. Additionally, IRG1 expression is reduced in TAMs, and IRG1-deficient mice exhibit accelerated tumor growth. Together, these findings support a protective role for endogenous itaconate in lung cancer. This spatial depletion was undetected in previous bulk analyses,[28,29] which suggests that IRG1-driven inflammatory programs are attenuated within tumors, thus raising important questions about the timing and regulation of IRG1 induction in lung cancer. Previous studies have shown that macrophages and myeloid cells upregulate IRG1 during pro-inflammatory processes,[30] which is a crucial response expected from anti-tumor macrophages in lung cancer.[6,8,9] Through a comprehensive analysis of internal and publicly available scRNA-seq datasets of mouse and human lung tumors, we confirmed not only that macrophages are the major cells responsible for IRG1 expression but also that the upregulation of IRG1 is accompanied by a more pronounced anti-tumor gene signature. The absence of IRG1 gene expression in The Cancer Genome Atlas (TCGA) data for lung cancer[31] and the limited number of IRG1-expressing cells in the scRNA-seq analysis could be due to insufficient sequencing depth or spatio-temporal regulation of multiple clusters of macrophages and monocytes in human and mouse lung tumors. We consider the latter to be very likely, as Casanova-Acebes et al.[32] have documented that monocyte-derived macrophages dominate advanced tumor lesions and that *Irg1* expression in macrophages gradually decreases during the progression of lung tumors in mice. Integrating our *in vitro* data from IRG1-deficient human and mouse macrophages with the findings of Casanova-Acebes et al. and Michelucci et al.[17] on IRG1 expression in tumor tissue and inflammatory contexts, we postulate that IRG1 gene expression follows bell-shaped kinetics during tumor development; there is an early increase as anti-tumor macrophages attempt to counteract tumor growth by releasing pro-inflammatory mediators, which is followed by a gradual decline as lung cancer progresses and anti-tumor macrophages are either replaced by or reprogrammed into pro-tumor macrophages. This notion is further supported by the observation that the survival benefit associated with higher ABCG2 expression is most pronounced in stage I lung adenocarcinoma. Although the mechanisms underlying the downregulation of IRG1 during tumor progression require further investigation, these data hint toward an anti-tumorigenic potential for IRG1.

Across multiple lung cancer models, IRG1 loss increased tumor burden, thus supporting an anti-tumor role for IRG1-expressing bone marrow-derived cells. At first glance, these findings contrast with studies in ovarian, melanoma, colorectal, and pancreatic cancers, where IRG1 has been attributed pro-tumor roles primarily through suppression of $CD8^+$ T cell activity.[33–36] However, other tumor contexts reported similar findings to our study in lung cancer: in breast cancer, itaconate restricts tumor proliferation and growth,[37] and in lymphoma, tumor-cell-intrinsic itaconate biosynthesis enhances antigen presentation and promotes $CD8^+$ T cell-mediated clearance.[38] Collectively, these divergent outcomes highlight that the IRG1/itaconate pathway is profoundly context-dependent and shaped by the immunometabolic landscape of each tissue. Our TCGA analysis further supports this concept, as it shows that high ABCG2 expression—a recently identified itaconate exporter—is associated with improved survival specifically in lung and breast cancers, which are the same cancer types in which itaconate exerts anti-tumor effects (HR < 1). This concordance between mechanistic and clinical data reinforces a model in which efficient itaconate export confers a survival advantage.

To understand why IRG1/itaconate exerts anti-tumor activity in lung cancer despite pro-tumor roles in several other malignancies, it is essential to consider the unique immunometabolic environment of the lung. The lung represents a unique microenvironment with a high baseline inflammatory tone, continuous antigen exposure, and a macrophage-driven epithelial defense program. Within this setting, IRG1-derived itaconate functions

(B) G6PD activity in M0, pro-, and anti-inflammatory macrophage, which were expressed relative to anti-inflammatory macrophages ($n = 3$ biological replicates for each group).
(C) Proliferation of A549 cells after 24 h of direct treatment with Octyl Ita and CM of anti-inflammatory macrophages treated with DMSO or Octyl Ita for 24 h ($n = 6$ biological replicates for each group).
(D and E) Reduced PPP intermediates and G6PD activity in anti-inflammatory macrophages after 12-h Octyl Ita treatment (n = 2–4 biological replicates for each group).
(F) Principal-component analysis (PCA) of transcriptomes from pro-inflammatory macrophages and anti-inflammatory macrophages treated with DMSO or Octyl Ita for 24 h ($n = 4$ biological replicates for each group).
(G) Pathway enrichment analysis comparing pro- vs. anti-inflammatory macrophages (left), Octyl Ita-treated vs. DMSO-treated anti-inflammatory macrophages (middle), and Octyl Ita-treated anti- vs. pro-inflammatory macrophages (right) ($n = 4$ biological replicates for each group).
(H and I) Proteomic volcano plot and pathway enrichment analysis of anti-inflammatory macrophages treated with Octyl Ita (250 μM) or DMSO for 24 h ($n = 4$ biological replicates for each group).
(J) Sankey plot summarizing significantly enriched pathways across transcriptomic and proteomic communities.
(K) A549 proliferation in CM from Octyl Ita-treated anti-inflammatory macrophages with or without PPP metabolite supplementation ($n = 3$ biological replicates for each group).
(L) Expression of pro-inflammatory (TNF and CD80) and anti-inflammatory (CSF1R and CD206) markers in anti-inflammatory macrophages transfected with siG6PD or siControl and treated with Octyl Ita or DMSO ($n = 5$ biological replicates for each group).
(M) Proliferation of A549 cells cultured in CM from siG6PD-transfected anti-inflammatory macrophages treated with Octyl Ita or DMSO ($n = 5$ biological replicates for each group).
Data are mean ± SEM. Statistical significance was determined by two-tailed unpaired Student's t test and one- and two-way ANOVA. ns, not significant; $^*p < 0.05$, $^{**}p < 0.01$, $^{***}p < 0.001$, and $^{****}p < 0.0001$.

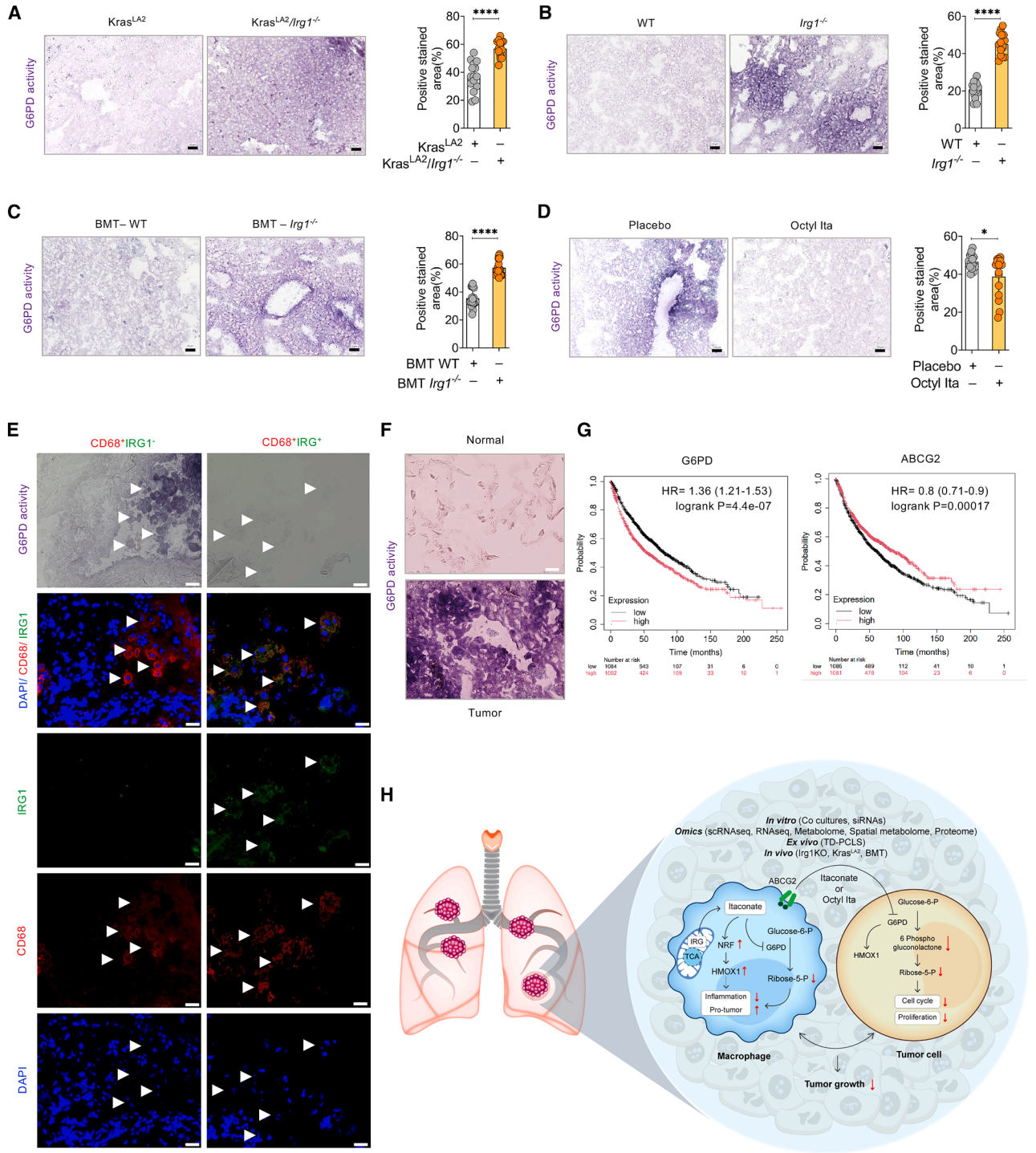


Figure 6. IRG1 and Octyl Ita reduce the G6PD activity in lung tumors

(A–D) Representative images of *in situ* G6PD activity in lungs of (A) Kras^{LA2} and Kras^{LA2}/*Irg1*$^{-/-}$ mice, (B) WT and *Irg1*$^{-/-}$ mice injected with LLC1 via the tail vein, (C) BMT WT and *Irg1*$^{-/-}$ mice injected with LLC1 via the tail vein, and (D) WT mice which were first injected with LLC1 cells via the tail vein and then treated with Octyl Ita (100 mg/kg) intraperitoneally every other day for 2 weeks (n = 15 technical replicates from 3 biological replicates for each group) (scale bar, 20 μm).

(E) Immunofluorescence staining for CD68 (red), IRG1 (green), and nuclei (blue) in human lung cancer sections, with corresponding *in situ* G6PD activity measured on the same slide. Scale bar, 10 μm.

(F) Representative images of *in situ* G6PD activity in human normal and tumor lung tissues (n = 3 biological replicates for each group).

(G) Kaplan-Meier survival analysis of lung adenocarcinoma patients stratified by G6PD and ABCG2 expression. HR, hazard ratio.

Data are mean ± SEM. Statistical significance was determined by two-tailed unpaired Student's t test. $p < 0.05$, $^{*}p < 0.01$, $^{**}p < 0.001$, and $^{***}p < 0.0001$.

(legend continued on next page)

as a metabolic regulator that maintains macrophages in a more pro-inflammatory, anti-tumor state. Supporting this, studies in chronic lung diseases including COPD, pulmonary fibrosis, and allergic asthma show that IRG1 deficiency skews macrophages toward an immunoregulatory, pro-fibrotic phenotype, which weakens epithelial protection and generates conditions that are permissive for tumorigenesis.[39,40] Consistent with this, we and others have observed a higher abundance of *Irg1*-expressing macrophages in the lung relative to other tissues, and clinical meta-analyses indicate that, in lung cancer, the balance between pro- and anti-inflammatory macrophages, rather than total macrophage number is a key determinant of patient outcome.[6,41,42] Together, these findings support a model in which the IRG1/itaconate axis sustains a lung-specific inflammatory-metabolic equilibrium that restrains tumor progression by maintaining anti-tumor macrophage function. However, given the context-dependent effects of itaconate in other malignancies, the therapeutic use of itaconate derivatives will require careful consideration of tumor origin, immune composition, and the cellular source of itaconate to avoid unintended pro-tumor consequences.[41]

Consistent with its dual role in macrophages and cancer cells, IRG1/itaconate deficiency promotes a tumor-supportive TAM phenotype as a key player in tumor development,[43] which links impaired macrophage anti-tumor activity to enhanced cancer cell proliferation.

Traditionally, itaconate has been thought to regulate tumor progression indirectly through macrophage-mediated paracrine effects. Challenging this view, we demonstrate that itaconate and its derivative Octyl Ita exert direct anti-proliferative effects on cancer cells across *in vitro*, *in vivo*, and *ex vivo* lung cancer models. Notably, itaconate exhibits an anti-proliferative effect on fibroblasts in pulmonary fibrosis contexts, and while Zhao et al. highlight *Irg1*'s pro-tumor role in melanoma, they also acknowledge itaconate's anti-proliferative effect on $CD4^+$ and $CD8^+$ T cells, which indicates a broad anti-proliferative attribute across tumor types.[34,39] The absence of IRG1 and itaconate production in epithelial cancer cells, together with the direct growth-inhibitory effects of exogenous itaconate, underscores the importance of macrophage-derived, extracellular itaconate in bidirectional macrophage-tumor cell crosstalk.[44] While previous studies have emphasized the cell-autonomous functions of intracellular itaconate, particularly in immune cells, our data support a model in which secreted itaconate may directly modulate the proliferation of adjacent cancer cells.[45] While extracellular itaconate concentrations are generally low, the local levels in macrophage-rich tumor niches may be higher due to paracrine release and restricted diffusion. Moreover, Octyl Ita efficiently elevates intracellular itaconate, such that our *in vitro* dosing likely reflects localized microenvironmental and/or pharmacologic exposure.

Our findings indicate that the anti-proliferative and immunomodulatory effects of IRG1/itaconate, including Octyl Ita, are linked to the inhibition of G6PD activity and consequently the modulation of PPP metabolism. This mechanism likely contributes to altered oxidative stress responses and reduced nucleotide biosynthesis.[46] While our detailed PPP flux analyses were performed in A549 cells, Octyl Ita suppressed proliferation across multiple lung cancer cell lines, which suggested that PPP/G6PD dependence may extend beyond a single model. Whether the extent of PPP sensitivity varies across additional genetic subtypes remains an important question for future studies. Prior work has shown that IRG1 can modulate macrophage redox signaling; for example, Liu et al.[47] reported that IRG1 influences MHC-I expression through a ROS-dependent STAT-TAP1 axis. However, that study did not implicate G6PD or the PPP in IRG1-dependent signaling. Our findings extend this concept by identifying G6PD inhibition as a direct and functionally central consequence of IRG1/itaconate activity, which links IRG1 to PPP suppression, NADPH limitation, and downstream metabolic-inflammatory rewiring in both macrophages and tumor cells.[47] Our *in silico* analyses show that itaconate binds directly within the G6PD catalytic pocket and suppresses maximal enzyme activity, yet we detect no evidence of the covalent modification of G6PD by itaconate in intact cells. Notably, recent work from Artyomov's group similarly demonstrated that itaconate regulates cellular redox status through non-covalent binding to the antioxidant enzyme PRDX5,[48] which supports an emerging model in which itaconate commonly acts through reversible interactions rather than covalent adduction.

In addition to this direct itaconate-G6PD interaction and the associated inhibition of G6PD activity, secreted itaconate may also act as a signaling metabolite by binding and activating the G-protein-coupled receptor OXGR1 on epithelial cells.[40] While we cannot rule out the potential role of itaconate/OXGR1 signaling in cancer cells and macrophages, our current findings regarding the direct inhibitory effect of itaconate on G6PD activity underscore the importance of its intracellular entry, where it can bind directly to G6PD. However, the mechanisms controlling the transport of itaconate from the extracellular to the intracellular environment and vice versa remain important unanswered questions in the biology of itaconate.

Of interest, we also found that itaconate/Octyl Ita modulates PPP metabolism and oxidative stress response in cancer cells in an NRF2-independent manner, while the effects of itaconate/Octyl Ita in macrophages are NRF2-dependent. Octyl Ita is known to activate NRF2 via cysteine modification of KEAP1 in activated macrophages.[19] NRF2 transcriptionally regulates genes such as G6PD, which are involved in PPP metabolism and oxidative stress response.[49] While we did not observe the activation of NRF2 and PPP-associated genes in cancer cells after treatment with IRG1/itaconate and Octyl Ita, oxidative stress-response genes were upregulated, which suggests an NRF2-independent mechanism but G6PD-dependent upregulation of oxidative stress-response genes (e.g., HMOX1). In contrast to cancer cells, as similarly shown by Mills et al.,[19] we

(H) Model of IRG1/itaconate-mediated metabolic control of macrophages and tumor cell function in lung cancer. IRG1-dependent itaconate production in anti-tumor macrophages inhibits G6PD activity, thus suppressing PPP flux and R5P availability, and so promotes NRF2/HMOX1-associated stress responses that limit pro-tumor polarization. Itaconate is exported via ABCG2 and acts non-cell-autonomously on tumor cells, where exogenous itaconate or Octyl Ita similarly inhibits G6PD, reduces PPP output and nucleotide synthesis, and suppresses proliferation. This IRG1/itaconate-G6PD axis restrains lung tumor growth across mouse models and human precision-cut lung slices, thus supporting its therapeutic potential.

observed NRF2 activation upon Octyl Ita treatment that was accompanied by the upregulation of genes involved in PPP metabolism and oxidative stress response in pro-tumor macrophages. This discrepancy could result from differences in the inflammatory/oxidative states of these cell types that influence the effects of itaconate on cellular oxidative responses. In support of this notion, Swain et al. have shown that the presence of inflammatory/oxidative conditions is critical for significant NRF2 induction by IRG1/itaconate.[14]

Recently, the PPP has been shown to play a critical role in cancer cell growth by providing both the nucleotide precursors required for proliferation and NADPH, which is used for both intracellular ROS detoxification and catabolic metabolism.[50] Key PPP enzymes, including G6PD, have a strong impact on cancer cell growth, and they are elevated in many human cancers and correlate with poor prognosis.[51] Notably, recent work highlights subtype-specific consequences of G6PD loss across lung cancer models, which indicates that metabolic dependencies on PPP activity may vary by genetic context. Our findings are consistent with a tumor-promoting role for G6PD in KRAS-driven and LLC1 models but do not exclude context-dependent effects in other lung cancer subtypes.[52] Therefore, the inhibition of PPP and/or G6PD inhibition has been proposed as an attractive therapeutic strategy against cancer. However, the inhibition of G6PD in a clinical setting is hampered by the lack of specific inhibitors.[49] Thus, itaconate/Octyl Ita, which modulates PPP metabolism and directly inhibits G6PD, may have potential therapeutic value. In our study, we found strong anti-tumor effects of itaconate in both *in vitro* and *in vivo* models of lung cancer. In addition, a strong anti-tumor effect was observed in itaconate-treated human lung slices from lung tumor tissue. In line with these findings, dimethyl itaconate and Octyl Ita have also been shown to have anti-tumor effects in colorectal and ovarian cancers, respectively.[53,54]

In summary, we present two novel findings on itaconate biology: first, the anti-tumor functions of IRG1/itaconate-expressing macrophages during lung tumorigenesis, and second, the inhibition of G6PD activity and PPP metabolism as the primary mechanisms underlying the anti-tumor effects of IRG1/itaconate and Octyl Ita. The novel inhibitory effects of IRG1/itaconate and Octyl Ita on G6PD activity and PPP metabolism not only drive the reeducation of pro-tumor macrophages into anti-tumor macrophages in a cell-autonomous manner but also provide direct suppression of cancer cell proliferation in a non-cell-autonomous manner. Finally, our results suggest that Octyl Ita is an effective anti-tumor metabolite with potential therapeutic application in lung cancer.

Limitations of the study

Although high-resolution MALDI-MSI revealed the spatial enrichment of itaconate within lung tumors, this approach does not allow direct cell-type attribution *in situ*. Single-cell analyses implicate macrophages as the primary source in the lung TME, but definitive spatial validation will require future methods. *In vivo* studies largely used Octyl Ita. Although genetic IRG1 gain- and loss-of-function models support the physiological relevance of endogenous itaconate, the differences in pharmacokinetics and cellular distribution between Octyl Ita and native itaconate should be considered. While G6PD inhibition and PPP suppression were shared mechanisms in cancer cells and macrophages, downstream redox responses differed, which indicated that there were additional cell-type-specific regulatory layers that remain to be defined. Although G6PD and ABCG2 expression were correlated with clinical outcomes, direct measurements of itaconate levels and G6PD activity in patient samples, particularly in the early disease stages, were not performed.

RESOURCE AVAILABILITY

Lead contact

Requests for further information and resources should be directed to and will be fulfilled by the lead contact, Rajkumar Savai rajkumar.savai@mpi-bn.mpg.de(savai.rajkumar@innere.med.uni-gieesen.de).

Materials availability

The materials that support the findings of this study are available from the lead contact upon reasonable request.

Data and code availability

The RNA-seq results are available in the NCBI's Gene Expression Omnibus (GEO) database (GEO: GSE256045). All data supporting the findings of this study are available within the article and its supplemental information.

ACKNOWLEDGMENTS

The authors thank Dr. Rajender Nandigama for helping with immunofluorescence (IF) quantification, Dr. Kati Turkowski for helping with the animal experiment proposal, and Yanina Buss, Jeanette Knepper, and Tim Schach for their excellent technical assistance. The authors acknowledge support from the Bruker Company, especially Dr. Andras Kiss, Dr. Jasmin Meltretter, Dr. Björn Wendik, Dr. Janina Oetjen, and Dr. Corinna Henkel for their support in MALDI-MSI. We also acknowledge Proteomics Biomedicum, the Karolinska Institute, and Dr. Akos Vegvary for acquiring the LC-MS/MS base quantitative proteomics data. This work was supported by the Max Planck Society; the Institute for Lung Health (ILH); the German Center for Lung Research (DZL); BMBF (KMU-innovativ-22: miRTumorProst; 031B0768C); Deutsche Forschungsgemeinschaft (DFG, German Research Foundation) grant nos. SA 1923/7-1 and SFB1213 (projects A01, A05, and A10N); the Excellence Cluster Cardiopulmonary Institute (EXC 2026: Cardio Pulmonary Institute (CPI), project 390649896); the State of Hesse (LOEWE iCANx, Projects A6, B4, B5, and Area C); a European Research Council (ERC) Consolidator Grant (grant no. 866051); Swedish Research Council grants 2018-06156, 2021-00993, and 2021-01756; the Austrian Science Fund (FWF) grant no. 10.55776/F8300; and the European Union's Horizon Research and Innovation Actions under grant agreement no. 101191315 (COMBAT).

AUTHOR CONTRIBUTIONS

R.S. and S.S.P. supervised the research. R.S., S.S.P., and S.M. conceptualized and designed the research. S.M., G.H., M.S., A.K., B.A., T.S., E.S.-F., and A.W. performed experiments and acquired data. S.M., G.H., S.S.P., C.K., U.N., A.A., and S. Guenther performed RNA-seq and analyzed and interpreted the results. A.H., A.M., B.P., and S.M. performed flux glucose analysis and interpreted the results. M.S. and S.M. performed LC-MS to check G6PD modification upon ITalK treatment and interpreted the results. S.Z., G.H., S.K., and I.F. performed MS metabolomics and interpreted the results. S.M., U.N., and A.A. performed proteomics and interpreted the results. S.M. and A.H. performed G6PD enzyme activity, B.A. and A.W. performed fluorescence-activated cell sorting (FACS) analysis, and K.B.K. performed *in silico* analysis of G6PD activity. F.G., C.R., I.A., M.R., and S. Gattenlöhner provided human samples. R.S. and S.S.P. acquired funding, and all authors participated in writing the manuscript.

DECLARATION OF INTERESTS

The authors declare that they have no competing interests.

DECLARATION OF GENERATIVE AI AND AI-ASSISTED TECHNOLOGIES IN THE WRITING PROCESS

During the preparation of this work, the authors used ChatGPT to grammatically edit the text. After using this tool, the authors reviewed and edited the content as needed and take full responsibility for the content of the publication.

STAR★METHODS

Detailed methods are provided in the online version of this paper and include the following:

- KEY RESOURCES TABLE
- EXPERIMENTAL MODEL AND STUDY PARTICIPANT DETAILS
  - Cell lines
  - Primary human Mϕ generation
  - Mouse Mϕ generation
  - Human lung tissues
  - Animal experiments
- METHOD DETAILS
  - Macrophage polarization and metabolite treatment
  - Transfection with siRNA and plasmid
  - RNA isolation, complementary DNA (cDNA) synthesis, and quantitative PCR
  - Western blotting
  - Proliferation and apoptosis assay
  - Magnetic-activated cell sorting (MACS)
  - Flow cytometry and cell sorting
  - Metabolome measurement via LC-MS/MS
  - Metabolic flux analysis
  - RNAseq analysis
  - Transcriptomics analysis
  - LC-MS/MS based quantitative proteomics
  - Integrative analysis
  - Olink assay
  - G6PD enzyme activity
  - Stable isotope tracing with 1,2-$^{13}C_2$-Glucose
  - MALDI-MSI Sample Preparation and Data Acquisition
  - G6PD modification with ITalk
  - GSH/GSSG measurement
  - In silico analysis of G6PD activity
  - Precision cut lung slices from human lung cancer patients
  - Immunofluorescence staining
  - Tumor cell injection
  - Bone marrow transplantation (BMT)
- QUANTIFICATION AND STATISTICAL ANALYSIS
  - Quantification
  - Statistical analysis

SUPPLEMENTAL INFORMATION

Supplemental information can be found online at https://doi.org/10.1016/j.cmet.2026.05.005.

Received: April 16, 2024
Revised: February 11, 2026
Accepted: May 8, 2026
Published: June 3, 2026

REFERENCES

1. Siegel, R.L., Miller, K.D., and Jemal, A. (2020). Cancer statistics, 2020. CA Cancer J. Clin. *70*, 7–30. https://doi.org/10.3322/caac.21590.
2. Siegel, R.L., Miller, K.D., Fuchs, H.E., and Jemal, A. (2021). Cancer statistics, 2021. CA Cancer J. Clin. *71*, 7–33. https://doi.org/10.3322/caac.21654.
3. Altorki, N.K., Markowitz, G.J., Gao, D., Port, J.L., Saxena, A., Stiles, B., McGraw, T., and Mittal, V. (2019). The lung microenvironment: an important regulator of tumour growth and metastasis. Nat. Rev. Cancer *19*, 9–31. https://doi.org/10.1038/s41568-018-0081-9.
4. Mansouri, S., Heylmann, D., Stiewe, T., Kracht, M., and Savai, R. (2022). Cancer genome and tumor microenvironment: Reciprocal crosstalk shapes lung cancer plasticity. eLife *11*, e79895. https://doi.org/10.7554/eLife.79895.
5. Jayasingam, S.D., Citartan, M., Thang, T.H., Mat Zin, A.A., Ang, K.C., and Ch'ng, E.S. (2019). Evaluating the polarization of tumor-associated macrophages into M1 and M2 phenotypes in human cancer tissue: technicalities and challenges in routine clinical practice. Front. Oncol. *9*, 1512. https://doi.org/10.3389/fonc.2019.01512.
6. Zheng, X., Weigert, A., Reu, S., Guenther, S., Mansouri, S., Bassaly, B., Gattenlöhner, S., Grimminger, F., Pullamsetti, S., Seeger, W., et al. (2020). Spatial density and distribution of tumor-associated macrophages predict survival in non-small cell lung carcinoma. Cancer Res. *80*, 4414–4425. https://doi.org/10.1158/0008-5472.CAN-20-0069.
7. Jackute, J., Zemaitis, M., Pranys, D., Sitkauskiene, B., Miliauskas, S., Vaitkiene, S., and Sakalauskas, R. (2018). Distribution of M1 and M2 macrophages in tumor islets and stroma in relation to prognosis of non-small cell lung cancer. BMC Immunol. *19*, 3. https://doi.org/10.1186/s12865-018-0241-4.
8. Sarode, P., Zheng, X., Giotopoulou, G.A., Weigert, A., Kuenne, C., Günther, S., Friedrich, A., Gattenlöhner, S., Stiewe, T., Brüne, B., et al. (2020). Reprogramming of tumor-associated macrophages by targeting beta-catenin/FOSL2/ARID5A signaling: A potential treatment of lung cancer. Sci. Adv. *6*, eaaz6105. https://doi.org/10.1126/sciadv.aaz6105.
9. Zheng, X., Sarode, P., Weigert, A., Turkowski, K., Chelladurai, P., Günther, S., Kuenne, C., Winter, H., Stenzinger, A., Reu, S., et al. (2023). The HDAC2-SP1 axis orchestrates protumor macrophage polarization. Cancer Res. *83*, 2345–2357. https://doi.org/10.1158/0008-5472.CAN-22-1270.
10. Xiao, H., Guo, Y., Li, B., Li, X., Wang, Y., Han, S., Cheng, D., and Shuai, X. (2020). M2-like tumor-associated macrophage-targeted codelivery of STAT6 inhibitor and IKKbeta siRNA induces M2-to-M1 repolarization for cancer immunotherapy with low immune side effects. ACS Cent. Sci. *6*, 1208–1222. https://doi.org/10.1021/acscentsci.9b01235.
11. Georgoudaki, A.M., Prokopec, K.E., Boura, V.F., Hellqvist, E., Sohn, S., Östling, J., Dahan, R., Harris, R.A., Rantalainen, M., Klevebring, D., et al. (2016). Reprogramming tumor-associated macrophages by antibody targeting inhibits cancer progression and metastasis. Cell Rep. *15*, 2000–2011. https://doi.org/10.1016/j.celrep.2016.04.084.
12. Russell, D.G., Huang, L., and VanderVen, B.C. (2019). Immunometabolism at the interface between macrophages and pathogens. Nat. Rev. Immunol. *19*, 291–304. https://doi.org/10.1038/s41577-019-0124-9.
13. Hooftman, A., and O'Neill, L.A.J. (2019). The immunomodulatory potential of the metabolite itaconate. Trends Immunol. *40*, 687–698. https://doi.org/10.1016/j.it.2019.05.007.
14. Swain, A., Bambouskova, M., Kim, H., Andhey, P.S., Duncan, D., Auclair, K., Chubukov, V., Simons, D.M., Roddy, T.P., Stewart, K.M., et al. (2020). Comparative evaluation of itaconate and its derivatives reveals divergent inflammasome and type I interferon regulation in macrophages. Nat. Metab. *2*, 594–602. https://doi.org/10.1038/s42255-020-0210-0.
15. Lampropoulou, V., Sergushichev, A., Bambouskova, M., Nair, S., Vincent, E.E., Loginicheva, E., Cervantes-Barragan, L., Ma, X., Huang, S.C.C., Griss, T., et al. (2016). Itaconate links inhibition of succinate dehydrogenase with macrophage metabolic remodeling and regulation of inflammation. Cell Metab. *24*, 158–166. https://doi.org/10.1016/j.cmet.2016.06.004.
16. Lee, C.G., Jenkins, N.A., Gilbert, D.J., Copeland, N.G., and O'Brien, W.E. (1995). Cloning and analysis of gene regulation of a novel LPS-inducible cDNA. Immunogenetics *41*, 263–270. https://doi.org/10.1007/BF00172150.

17. Michelucci, A., Cordes, T., Ghelfi, J., Pailot, A., Reiling, N., Goldmann, O., Binz, T., Wegner, A., Tallam, A., Rausell, A., et al. (2013). Immune-responsive gene 1 protein links metabolism to immunity by catalyzing itaconic acid production. Proc. Natl. Acad. Sci. USA *110*, 7820–7825. https://doi.org/10.1073/pnas.1218599110.

18. Liao, S.T., Han, C., Xu, D.Q., Fu, X.W., Wang, J.S., and Kong, L.Y. (2019). 4-Octyl itaconate inhibits aerobic glycolysis by targeting GAPDH to exert anti-inflammatory effects. Nat. Commun. *10*, 5091. https://doi.org/10.1038/s41467-019-13078-5.

19. Mills, E.L., Ryan, D.G., Prag, H.A., Dikovskaya, D., Menon, D., Zaslona, Z., Jedrychowski, M.P., Costa, A.S.H., Higgins, M., Hams, E., et al. (2018). Itaconate is an anti-inflammatory metabolite that activates Nrf2 via alkylation of KEAP1. Nature *556*, 113–117. https://doi.org/10.1038/nature25986.

20. Chen, L.L., Morcelle, C., Cheng, Z.L., Chen, X., Xu, Y., Gao, Y., Song, J., Li, Z., Smith, M.D., Shi, M., et al. (2022). Itaconate inhibits TET DNA dioxygenases to dampen inflammatory responses. Nat. Cell Biol. *24*, 353–363. https://doi.org/10.1038/s41556-022-00853-8.

21. Nelson, V.L., Nguyen, H.C.B., Garcìa-Cañaveras, J.C., Briggs, E.R., Ho, W.Y., DiSpirito, J.R., Marinis, J.M., Hill, D.A., and Lazar, M.A. (2018). PPARgamma is a nexus controlling alternative activation of macrophages via glutamine metabolism. Genes Dev. *32*, 1035–1044. https://doi.org/10.1101/gad.312355.118.

22. Ganta, V.C., Choi, M.H., Kutateladze, A., Fox, T.E., Farber, C.R., and Annex, B.H. (2017). A MicroRNA93-interferon regulatory factor-9-immunoresponsive gene-1-itaconic acid pathway modulates M2-like macrophage polarization to revascularize ischemic muscle. Circulation *135*, 2403–2425. https://doi.org/10.1161/CIRCULATIONAHA.116.025490.

23. Runtsch, M.C., Angiari, S., Hooftman, A., Wadhwa, R., Zhang, Y., Zheng, Y., Spina, J.S., Ruzek, M.C., Argiriadi, M.A., McGettrick, A.F., et al. (2022). Itaconate and itaconate derivatives target JAK1 to suppress alternative activation of macrophages. Cell Metab. *34*, 487–501.e8. https://doi.org/10.1016/j.cmet.2022.02.002.

24. Weigert, A., Zheng, X., Nenzel, A., Turkowski, K., Günther, S., Strack, E., Sirait-Fischer, E., Elwakeel, E., Kur, I.M., Nikam, V.S., et al. (2022). Fibrocytes boost tumor-supportive phenotypic switches in the lung cancer niche via the endothelin system. Nat. Commun. *13*, 6078. https://doi.org/10.1038/s41467-022-33458-8.

25. Kim, N., Kim, H.K., Lee, K., Hong, Y., Cho, J.H., Choi, J.W., Lee, J.I., Suh, Y.L., Ku, B.M., Eum, H.H., et al. (2020). Single-cell RNA sequencing demonstrates the molecular and cellular reprogramming of metastatic lung adenocarcinoma. Nat. Commun. *11*, 2285. https://doi.org/10.1038/s41467-020-16164-1.

26. Zilionis, R., Engblom, C., Pfirschke, C., Savova, V., Zemmour, D., Saatcioglu, H.D., Krishnan, I., Maroni, G., Meyerovitz, C.V., Kerwin, C.M., et al. (2019). Single-cell transcriptomics of human and mouse lung cancers reveals conserved myeloid populations across individuals and species. Immunity *50*, 1317–1334.e10. https://doi.org/10.1016/j.immuni.2019.03.009.

27. Karger, A., Mansouri, S., Leisegang, M.S., Weigert, A., Günther, S., Kuenne, C., Wittig, I., Zukunft, S., Klatt, S., Aliraj, B., et al. (2023). ADPGK-AS1 long noncoding RNA switches macrophage metabolic and phenotypic state to promote lung cancer growth. EMBO J. *42*, e111620. https://doi.org/10.15252/embj.2022111620.

28. Che, M., Wei, W., Yang, X., Liang, J., Li, Y., Ye, Y., Sun, Y., Hu, Y., Zhang, Z., Qin, Y., et al. (2025). Radiation-induced upregulation of itaconate in macrophages promotes the radioresistance of non-small cell lung cancer by stabilizing NRF2 protein and suppressing immune response. Redox Biol. *85*, 103711. https://doi.org/10.1016/j.redox.2025.103711.

29. Gu, X., Wei, H., Suo, C., Shen, S., Zhu, C., Chen, L., Yan, K., Li, Z., Bian, Z., Zhang, P., et al. (2023). Itaconate promotes hepatocellular carcinoma progression by epigenetic induction of CD8+ T-cell exhaustion. Nat. Commun. *14*, 8154. https://doi.org/10.1038/s41467-023-43988-4.

30. Peace, C.G., and O'Neill, L.A. (2022). The role of itaconate in host defense and inflammation. J. Clin. Investig. *132*, e148548. https://doi.org/10.1172/JCI148548.

31. Goldman, M.J., Craft, B., Hastie, M., Repečka, K., McDade, F., Kamath, A., Banerjee, A., Luo, Y., Rogers, D., Brooks, A.N., et al. (2020). Visualizing and interpreting cancer genomics data via the Xena platform. Nat. Biotechnol. *38*, 675–678. https://doi.org/10.1038/s41587-020-0546-8.

32. Casanova-Acebes, M., Dalla, E., Leader, A.M., LeBerichel, J., Nikolic, J., Morales, B.M., Brown, M., Chang, C., Troncoso, L., Chen, S.T., et al. (2021). Tissue-resident macrophages provide a pro-tumorigenic niche to early NSCLC cells. Nature *595*, 578–584. https://doi.org/10.1038/s41586-021-03651-8.

33. Weiss, J.M., Davies, L.C., Karwan, M., Ileva, L., Ozaki, M.K., Cheng, R.Y., Ridnour, L.A., Annunziata, C.M., Wink, D.A., and McVicar, D.W. (2018). Itaconic acid mediates crosstalk between macrophage metabolism and peritoneal tumors. J. Clin. Investig. *128*, 3794–3805. https://doi.org/10.1172/JCI99169.

34. Zhao, H., Teng, D., Yang, L., Xu, X., Chen, J., Jiang, T., Feng, A.Y., Zhang, Y., Frederick, D.T., Gu, L., et al. (2022). Myeloid-derived itaconate suppresses cytotoxic CD8+ T cells and promotes tumour growth. Nat. Metab. *4*, 1660–1673. https://doi.org/10.1038/s42255-022-00676-9.

35. Chen, Y.J., Li, G.N., Li, X.J., Wei, L.X., Fu, M.J., Cheng, Z.L., Yang, Z., Zhu, G.Q., Wang, X.D., Zhang, C., et al. (2023). Targeting IRG1 reverses the immunosuppressive function of tumor-associated macrophages and enhances cancer immunotherapy. Sci. Adv. *9*, eadg0654. https://doi.org/10.1126/sciadv.adg0654.

36. Wang, X., Su, S., Zhu, Y., Cheng, X., Cheng, C., Chen, L., Lei, A., Zhang, L., Xu, Y., Ye, D., et al. (2023). Metabolic reprogramming via ACOD1 depletion enhances function of human induced pluripotent stem cell-derived CAR-macrophages in solid tumors. Nat. Commun. *14*, 5778. https://doi.org/10.1038/s41467-023-41470-9.

37. Wang, H.C., Chang, W.C., Lee, D.Y., Li, X.G., and Hung, M.C. (2023). IRG1/Itaconate induces metabolic reprogramming to suppress ER-positive breast cancer cell growth. Am. J. Cancer Res. *13*, 1067–1081.

38. Chen, F., Dowerg, B., and Cordes, T. (2023). The yin and yang of itaconate metabolism and its impact on the tumor microenvironment. Curr. Opin. Biotechnol. *84*, 102996. https://doi.org/10.1016/j.copbio.2023.102996.

39. Ogger, P.P., Albers, G.J., Hewitt, R.J., O'Sullivan, B.J., Powell, J.E., Calamita, E., Ghai, P., Walker, S.A., McErlean, P., Saunders, P., et al. (2020). Itaconate controls the severity of pulmonary fibrosis. Sci. Immunol. *5*, eabc1884. https://doi.org/10.1126/sciimmunol.abc1884.

40. Zeng, Y.R., Song, J.B., Wang, D., Huang, Z.X., Zhang, C., Sun, Y.P., Shu, G., Xiong, Y., Guan, K.L., Ye, D., et al. (2023). The immunometabolite itaconate stimulates OXGR1 to promote mucociliary clearance during the pulmonary innate immune response. J. Clin. Investig. *133*, e160463. https://doi.org/10.1172/JCI160463.

41. Larionova, I., Tuguzbaeva, G., Ponomaryova, A., Stakheyeva, M., Cherdyntseva, N., Pavlov, V., Choinzonov, E., and Kzhyshkowska, J. (2020). Tumor-associated macrophages in human breast, colorectal, lung, ovarian and prostate cancers. Front. Oncol. *10*, 566511. https://doi.org/10.3389/fonc.2020.566511.

42. Garrido-Martin, E.M., Mellows, T.W.P., Clarke, J., Ganesan, A.P., Wood, O., Cazaly, A., Seumois, G., Chee, S.J., Alzetani, A., King, E.V., et al. (2020). M1hot tumor-associated macrophages boost tissue-resident memory T cells infiltration and survival in human lung cancer. J. Immunother. Cancer *8*, e000778. https://doi.org/10.1136/jitc-2020-000778.

43. Mantovani, A., Allavena, P., Marchesi, F., and Garlanda, C. (2022). Macrophages as tools and targets in cancer therapy. Nat. Rev. Drug Discov. *21*, 799–820. https://doi.org/10.1038/s41573-022-00520-5.

44. Zheng, X., Mansouri, S., Krager, A., Grimminger, F., Seeger, W., Pullamsetti, S.S., Wheelock, C.E., and Savai, R. (2020). Metabolism in tumour-associated macrophages: a quid pro quo with the tumour microenvironment. Eur. Respir. Rev. *29*, 200134. https://doi.org/10.1183/16000617.0134-2020.

45. Strelko, C.L., Lu, W., Dufort, F.J., Seyfried, T.N., Chiles, T.C., Rabinowitz, J.D., and Roberts, M.F. (2011). Itaconic acid is a mammalian metabolite

induced during macrophage activation. J. Am. Chem. Soc. *133*, 16386–16389. https://doi.org/10.1021/ja2070889.

46. Stincone, A., Prigione, A., Cramer, T., Wamelink, M.M.C., Campbell, K., Cheung, E., Olin-Sandoval, V., Grüning, N.M., Krüger, A., Tauqeer Alam, M., et al. (2015). The return of metabolism: biochemistry and physiology of the pentose phosphate pathway. Biol. Rev. Camb. Philos. Soc. *90*, 927–963. https://doi.org/10.1111/brv.12140.
47. Liu, X., Wu, X.P., Zhu, X.L., Li, T., and Liu, Y. (2017). IRG1 increases MHC class I level in macrophages through STAT-TAP1 axis depending on NADPH oxidase mediated reactive oxygen species. Int. Immunopharmacol. *48*, 76–83. https://doi.org/10.1016/j.intimp.2017.04.012.
48. Paulenda, T., Echalar, B., Potuckova, L., Vachova, V., Kleverov, D.A., Mehringer, J., Potekhina, E., Jacoby, A., Sen, D., Nelson, C., et al. (2025). Itaconate modulates immune responses via inhibition of peroxiredoxin 5. Nat. Metab. *7*, 1183–1203. https://doi.org/10.1038/s42255-025-01275-0.
49. Mitsuishi, Y., Taguchi, K., Kawatani, Y., Shibata, T., Nukiwa, T., Aburatani, H., Yamamoto, M., and Motohashi, H. (2012). Nrf2 redirects glucose and glutamine into anabolic pathways in metabolic reprogramming. Cancer Cell *22*, 66–79. https://doi.org/10.1016/j.ccr.2012.05.016.
50. Zheng, P., Lin, Z., Ding, Y., and Duan, S. (2023). Targeting the dynamics of cancer metabolism in the era of precision oncology. Metabolism *145*, 155615. https://doi.org/10.1016/j.metabol.2023.155615.
51. Nagashio, R., Oikawa, S., Yanagita, K., Hagiuda, D., Kuchitsu, Y., Igawa, S., Naoki, K., Satoh, Y., Ichinoe, M., Murakumo, Y., et al. (2019). Prognostic significance of G6PD expression and localization in lung adenocarcinoma. Biochim. Biophys. Acta Proteins Proteom. *1867*, 38–46. https://doi.org/10.1016/j.bbapap.2018.05.005.
52. Lan, T., Arastu, S., Lam, J., Kim, H., Wang, W., Wang, S., Bhatt, V., Lopes, E.C., Hu, Z., Sun, M., et al. (2024). Glucose-6-phosphate dehydrogenase maintains redox homeostasis and biosynthesis in LKB1-deficient KRAS-driven lung cancer. Nat. Commun. *15*, 5857. https://doi.org/10.1038/s41467-024-50157-8.
53. Wang, Q., Li, X.L., Mei, Y., Ye, J.C., Fan, W., Cheng, G.H., Zeng, M.S., and Feng, G.K. (2020). The anti-inflammatory drug dimethyl itaconate protects against colitis-associated colorectal cancer. J. Mol. Med. (Berl.) *98*, 1457–1466. https://doi.org/10.1007/s00109-020-01963-2.
54. Zhan, Z., Wang, Z., Bao, Y., Liu, W., and Hong, L. (2022). OI inhibits development of ovarian cancer by blocking crosstalk between cancer cells and macrophages via HIF-1alpha pathway. Biochem. Biophys. Res. Commun. *606*, 142–148. https://doi.org/10.1016/j.bbrc.2022.03.106.
55. Johnson, L., Mercer, K., Greenbaum, D., Bronson, R.T., Crowley, D., Tuveson, D.A., and Jacks, T. (2001). Somatic activation of the K-ras oncogene causes early onset lung cancer in mice. Nature *410*, 1111–1116. https://doi.org/10.1038/35074129.
56. Wang, Y., Armando, A.M., Quehenberger, O., Yan, C., and Dennis, E.A. (2014). Comprehensive ultra-performance liquid chromatographic separation and mass spectrometric analysis of eicosanoid metabolites in human samples. J. Chromatogr. A *1359*, 60–69. https://doi.org/10.1016/j.chroma.2014.07.006.
57. Dobin, A., Davis, C.A., Schlesinger, F., Drenkow, J., Zaleski, C., Jha, S., Batut, P., Chaisson, M., and Gingeras, T.R. (2013). STAR: ultrafast universal RNA-seq aligner. Bioinformatics *29*, 15–21. https://doi.org/10.1093/bioinformatics/bts635.
58. Liao, Y., Smyth, G.K., and Shi, W. (2014). featureCounts: an efficient general purpose program for assigning sequence reads to genomic features. Bioinformatics *30*, 923–930. https://doi.org/10.1093/bioinformatics/btt656.
59. Love, M.I., Huber, W., and Anders, S. (2014). Moderated estimation of fold change and dispersion for RNA-seq data with DESeq2. Genome Biol. *15*, 550. https://doi.org/10.1186/s13059-014-0550-8.
60. Ritchie, M.E., Phipson, B., Wu, D., Hu, Y., Law, C.W., Shi, W., and Smyth, G.K. (2015). limma powers differential expression analyses for RNA-sequencing and microarray studies. Nucleic Acids Res. *43*, e47. https://doi.org/10.1093/nar/gkv007.
61. Krishnan, S., Nordqvist, H., Ambikan, A.T., Gupta, S., Sperk, M., Svensson-Akusjärvi, S., Mikaeloff, F., Benfeitas, R., Saccon, E., Ponnan, S.M., et al. (2021). Metabolic perturbation associated with COVID-19 disease severity and SARS-CoV-2 replication. Mol. Cell. Proteomics *20*, 100159. https://doi.org/10.1016/j.mcpro.2021.100159.
62. Willforss, J., Chawade, A., and Levander, F. (2019). NormalyzerDE: online tool for improved normalization of omics expression data and high-sensitivity differential expression analysis. J. Proteome Res. *18*, 732–740. https://doi.org/10.1021/acs.jproteome.8b00523.
63. Traag, V.A., Waltman, L., and van Eck, N.J. (2019). From Louvain to Leiden: guaranteeing well-connected communities. Sci. Rep. *9*, 5233. https://doi.org/10.1038/s41598-019-41695-z.
64. Chen, E.Y., Tan, C.M., Kou, Y., Duan, Q., Wang, Z., Meirelles, G.V., Clark, N.R., and Ma'ayan, A. (2013). Enrichr: interactive and collaborative HTML5 gene list enrichment analysis tool. BMC Bioinform. *14*, 128. https://doi.org/10.1186/1471-2105-14-128.
65. Subramanian, A., Tamayo, P., Mootha, V.K., Mukherjee, S., Ebert, B.L., Gillette, M.A., Paulovich, A., Pomeroy, S.L., Golub, T.R., Lander, E.S., et al. (2005). Gene set enrichment analysis: a knowledge-based approach for interpreting genome-wide expression profiles. Proc. Natl. Acad. Sci. USA *102*, 15545–15550. https://doi.org/10.1073/pnas.0506580102.
66. Gu, Z., Eils, R., and Schlesner, M. (2016). Complex heatmaps reveal patterns and correlations in multidimensional genomic data. Bioinformatics *32*, 2847–2849. https://doi.org/10.1093/bioinformatics/btw313.
67. Miller, A., Nagy, C., Knapp, B., Laengle, J., Ponweiser, E., Groeger, M., Starkl, P., Bergmann, M., Wagner, O., and Haschemi, A. (2017). Exploring metabolic configurations of single cells within complex tissue microenvironments. Cell Metab. *26*, 788–800.e6. https://doi.org/10.1016/j.cmet.2017.08.014.
68. Xia, J., Sinelnikov, I.V., Han, B., and Wishart, D.S. (2015). MetaboAnalyst 3.0–making metabolomics more meaningful. Nucleic Acids Res. *43*, W251–W257. https://doi.org/10.1093/nar/gkv380.
69. Heinrich, P., Kohler, C., Ellmann, L., Kuerner, P., Spang, R., Oefner, P.J., and Dettmer, K. (2018). Correcting for natural isotope abundance and tracer impurity in MS-, MS/MS- and high-resolution-multiple-tracer-data from stable isotope labeling experiments with IsoCorrectoR. Sci. Rep. *8*, 17910. https://doi.org/10.1038/s41598-018-36293-4.
70. Cairns, J.L., Huber, J., Lewen, A., Jung, J., Maurer, S.J., Bausbacher, T., Schmidt, S., Levkin, P.A., Sevin, D., Göpfrich, K., et al. (2025). Mass-guided single-cell MALDI imaging of low-mass metabolites reveals cellular activation markers. Adv. Sci. (Weinh) *12*, e2410506. https://doi.org/10.1002/advs.202410506.
71. Wang, G., Heijs, B., Kostidis, S., Mahfouz, A., Rietjens, R.G.J., Bijkerk, R., Koudijs, A., van der Pluijm, L.A.K., van den Berg, C.W., Dumas, S.J., et al. (2022). Analyzing cell-type-specific dynamics of metabolism in kidney repair. Nat. Metab. *4*, 1109–1118. https://doi.org/10.1038/s42255-022-00615-8.
72. Roquid, K.A., Vucetic, A., Dyukova, E., Hanssen, M.J., Cho, H., Bonnavion, R., Mattonet, K., Looso, M., Sanda, M., Strilic, B., et al. (2025). Lung endothelial PEAR1 induces tumor cell dormancy. Mol. Cancer *24*, 278. https://doi.org/10.1186/s12943-025-02488-3.
73. Mansouri, S., Karger, A., Ruppert, C., Schneider, M.A., Weigert, A., Nandigama, R., Aliraj, B., Strotmann, L., Cherian, A.V., Pruefer, D., et al. (2025). Living human lung slices for ex vivo modelling of lung cancer. JCI Insight *10*, e190703. https://doi.org/10.1172/jci.insight.190703.
74. Schmall, A., Al-Tamari, H.M., Herold, S., Kampschulte, M., Weigert, A., Wietelmann, A., Vipotnik, N., Grimminger, F., Seeger, W., Pullamsetti, S.S., et al. (2015). Macrophage and cancer cell cross-talk via CCR2 and CX3CR1 is a fundamental mechanism driving lung cancer. Am. J. Respir. Crit. Care Med. *191*, 437–447. https://doi.org/10.1164/rccm.201406-1137OC.

STAR★METHODS

KEY RESOURCES TABLE

REAGENT or RESOURCE	SOURCE	IDENTIFIER
Antibodies		
Antibodies information listed in Table S3	This study	N/A
Chemicals, peptides, and recombinant proteins		
Octyl itaconate (Octyl Ita)	Cayman	Cat# 25374
Itaconate (itaconic acid)	Sigma	Cat# 129204
LPS	Sigma	Cat# L5418
IFNγ	R and D Systems	Cat# 285-IF
IL-4	R and D Systems	Cat# 204-IL
M-CSF	R and D Systems	Cat# 416-ML
N-acetyl cysteine (NAC)	Sigma	Cat# A9165
6-phosphogluconate (6GP)	Sigma	Cat# P7877
D-ribose (DR)	Sigma	Cat# R9629
Ribose-5-phosphate (R5P)	Sigma	Cat# R7750
2-hydroxypropyl-β-cyclodextrin	Sigma	Cat# H107
Recombinant human G6PD	Abcam	Cat# ab167987
ITalk probe	Chomix Biotech	Cat# CMX210035
Cycloheximide	Sigma-Aldrich	Cat# C4859
[1,2-13C2]-glucose	Sigma	Cat# 453188
1,5-diaminonaphthalene (DAN)	Merc	Cat# 56451
HiPerFect	Qiagen	Cat# 371707
Critical commercial assays		
LookOut Mycoplasma PCR Detection Kit	Merck	MP0040A
RNeasy Mini Kit	Qiagen	Cat# 74104
miRNeasy Micro Kit	Qiagen	Cat# 217084
High-Capacity cDNA Reverse Transcription Kit	Applied Biosystems	Cat# 4368814
SYBR Green PCR Master Mix	Applied Biosystems	Cat# A25742
BrdU proliferation assay kit	Roche	Cat# 11647229001
Cell Death Detection ELISA kit	Roche	Cat# 11920685001
Tumor Dissociation Kit	Miltenyi Biotec	Cat# 130-095-929
CD68-PE antibody (MACS)	Miltenyi Biotec	Cat# 130-096-807
Anti-PE MicroBeads	Miltenyi Biotec	Cat# 130-048-801
GSH/GSSG-Glo assay	Promega	Cat# V6611
Deposited data		
RNA-seq	NCBI GEO	GSE256045
Experimental models: Cell lines		
A549	ATCC	CCL-185
H838	ATCC	CRL-5844
H1975	ATCC	CRL-5908
H1650	ATCC	CRL-5883
H226	ATCC	CRL-5826
LLC1	ATCC	CRL-1642
Experimental models: Organisms/strains		
C57BL/6 mice	Jackson Laboratory	N/A
Irg1$^{-/-}$ mice	Jackson Laboratory	N/A

(*Continued on next page*)

Continued

REAGENT or RESOURCE	SOURCE	IDENTIFIER
$Kras^{LA2}$ mice	Charles River	N/A
Oligonucleotides		
Human IRG1 siRNA (Hs_IRG1_4)	Qiagen	SI05379920
Human IRG1 siRNA (Hs_IRG1_3)	Qiagen	SI05172685
Human G6PD siRNA (Hs_G6PD_6)	Qiagen	SI03082450
Human G6PD siRNA (Hs_G6PD_2)	Qiagen	SI00008862
AllStars Negative Control siRNA	Qiagen	Cat# 1027292
qPCR primers	This study	Table S2
Recombinant DNA		
IRG1 overexpression plasmid	GeneCopoeia	Cat# Ex-I1206-Lv105
Empty control plasmid	GeneCopoeia	Cat# Ex-NEG-Lv105
TKT overexpression plasmid	Addgene	Cat# Plasmid #175331
Software and algorithms		
GraphPad Prism	GraphPad	v9
ImageJ	NIH	1.54P
SCiLS Lab	Bruker	2025b
MetaboScape	Bruker	2025

EXPERIMENTAL MODEL AND STUDY PARTICIPANT DETAILS

Cell lines

Various human cell lines (A549, H838, H1975, H1650, H226) and mouse LLC1 cells were obtained from the American Type Culture Collection (ATCC, Manassas, USA) and maintained according to ATCC guidelines. A549 cells were cultured in Dulbecco's modified Eagle's medium with 10% FCS and 1% P/S, while the other human cell lines and LLC1 cells were cultured in RPMI 1640 medium with 10% FCS and 1% P/S. All cells were maintained at 37°C in a humidified incubator with 5% CO_2. Cell line identity was based on the authentication provided by ATCC, and no additional authentication was performed after receipt. The mycoplasma test was performed using the LookOut Mycoplasma PCR Detection Kit (Merck, Darmstadt, Germany).

Primary human Mϕ generation

Human Mϕ were generated from peripheral blood mononuclear cells (PBMCs) as previously described.[6,8] Briefly, PBMCs were isolated from buffy coats obtained from the blood bank of the Universities of Giessen and Marburg Lung Center using Ficoll density gradient centrifugation. Platelets and red blood cells were removed by two washing steps with RBC lysis buffer (BD Biosciences) and phosphate buffered saline (PBS). The PBMCs were then seeded on 6-well plates (Sarstedt, Nümbrecht, Germany) in RPMI 1640 medium containing 1% P/S. After 2 hours, the non-adherent cells were removed and the remaining adherent cells were differentiated into Mϕ over 10 days in macrophage complete medium (RPMI 1640 medium with 2% human serum and 1% P/S).

Mouse Mϕ generation

For the isolation and differentiation of mouse Mϕ, tibia and femur were dissected, rinsed with 15 ml RPMI 1640 medium with 1% P/S and the cell suspension was passed through a 100-µm cell strainer. After centrifugation at 500 g for 10 min, the cell pellet was re-suspended in RPMI-1640 medium containing 10 % FCS, 1% P/S and mouse macrophage colony-stimulating factor (M-CSF) (20 ng/ml; Roche). The cells were seeded on a six-well plate and the medium was changed on alternate days with RPMI 1640 medium containing 10% FCS, 1% Pen/Strep and mouse M-CSF (20 ng/ml) until differentiated Mϕ were obtained after 5–6 days.

Human lung tissues

Human lung tumor and non-tumor part tissue samples were obtained in RPMI medium supplemented with 10 µg/ml cycloheximide (C4859, Sigma-Aldrich, St. Louis, USA). Samples were stored at 4 °C until the start of cell isolation on the same day. A written declaration of consent was obtained from each patient (ethical reference number: AZ 58/15). The study protocol for tissue donation was approved by the Ethics Committee of the Department of Human Medicine at Justus Liebig University Giessen'' in compliance with national regulations and the guidelines.

Animal experiments

The animal experiments conducted for this research were approved by the local authorities (Regierungspraesidium Darmstadt, Hessen, Germany). Mice, including C57BL/6 and *Irg1*$^{-/-}$ mice (7–8 weeks old) and $Kras^{LA2}$ transgenic mice (3–5 months old), were

treated according to European Commission guidelines for laboratory animals. Kras^{LA2} mice develop alveolar adenomatous hyperplasia 1 week after birth.[55] The *Irg1*$^{-/-}$ and Kras^{LA2} mice were obtained from Charles River Laboratories or Jackson Laboratory. Animals were housed under specific pathogen-free (SPF) conditions in a temperature-controlled facility (22 ± 2°C) with 50%–60% humidity, maintained on a 12-hour light/dark cycle, and provided with standard chow diet and water ad libitum. Mice were housed in groups (2–5 animals per cage) unless otherwise required by experimental procedures. Both male and female mice were used in this study unless otherwise specified.

METHOD DETAILS

Macrophage polarization and metabolite treatment

For macrophage polarization, pro-inflammatory Mϕ were generated by stimulating unpolarized Mϕ (M0) with LPS (100 ng/ml, Sigma) and interferon γ (IFNɣ) (100 U/ml, Roche) for 6 or 24 hours as indicated. Anti-inflammatory Mϕ were generated by treating M0 Mϕs with IL-4 (20 ng/ml; VWR, Radnor, USA) for 24 hours. The pH of the medium was checked after dissolution of the metabolites and adjusted to 7.2–7.5 before treatment of the cells.

To provide clarity on the experimental design and the rationale behind different Octyl Ita exposure times, we summarized all timing conditions across assays in Table S1. Early time points (6–12 hours) were selected to capture rapid metabolic responses, as metabolomics and redox measurements are highly sensitive to immediate biochemical perturbations that occur before transcriptional or proteomic remodeling. In contrast, later time points (24–48 hours) were used for transcriptomic and proteomic analyses to examine the downstream consequences of early metabolic inhibition, reflecting slower processes such as changes in gene expression, protein abundance, and pathway-level reprogramming. This tiered timing strategy allowed us to distinguish acute metabolic effects from later transcriptional and phenotypic adaptations.

Transfection with siRNA and plasmid

Transfection of Mϕ and A549 cells was performed with HiPerFect transfection reagent (Qiagen, Hilden, Germany) in serum-free Opti-MEM medium (Sigma-Aldrich, Taufkirchen, Germany). SiRNAs targeting IRG1 and G6PD, as well as AllStars negative siRNA (siControl), were purchased from Qiagen. Specific siRNA sequences included Hs_IRG1_4, (catalogue number: SI05379920), Hs_IRG1_3 (catalogue number: SI05172685), Hs_G6PD_6 (catalogue number: SI03082450) and Hs_G6PD_2 (catalogue number: SI00008862). Transfection was performed according to the manufacturer's protocol, starting in Opti-MEM medium for 6 hours, followed by the addition of complete medium for a further 24 or 48 hours.

A549 and H1650 cells were transfected with the IRG1-overexpressing plasmid (catalogue number: Ex-I1206-Lv105), TKT-overexpressing plasmid (catalogue number: 175331 from addgene) and the empty control plasmid (catalogue number: Ex-NEG-Lv105) from GeneCopoeia (Rockville, MD, USA) using TurboFect transfection reagent (Fermentas, Waltham, USA). Transfection included 1 μg of each plasmid in parallel, according to the protocol, and cells were incubated for 24 hours or longer as indicated.

RNA isolation, complementary DNA (cDNA) synthesis, and quantitative PCR

RNA was isolated using the RNeasy Mini Kit (Qiagen, Hilden, Germany),[6,8] followed by cDNA synthesis with the high-capacity cDNA reverse transcription Kit (Applied Biosystems, Waltham, USA). Quantitative PCR (qPCR) was conducted using SYBR Green PCR Master Mix and the StepOne real-time PCR System (Applied Biosystems, Waltham, USA) under specific conditions. Analysis employed StepOne plus software and GraphPad Prism, with expression determined through the ΔΔCT method and fold change calculation. CT-values were normalized to the housekeeping gene HPRT1 ($\Delta CT = CT_{reference} - CT_{target}$). Primer sequences were designed using NCBI database information and obtained from Sigma-Aldrich (see Table S2).

Western blotting

For western blotting, the Mϕ and A549 cells were lysed in RIPA buffer with protease and phosphatase inhibitors. The resulting lysates were centrifuged at 12,000 g for 15 minutes at 4 °C. The heat-denatured proteins were separated on 10% SDS-polyacrylamide gels and subsequently transferred to polyvinylidene difluoride membranes. After blocking with 5 % BSA in TBST, the membranes were incubated overnight at 4 °C with a primary antibody (1:1000 dilution in 5 % BSA/TBST). After washing three times with TBST, the blots were incubated with HRP-conjugated secondary antibodies diluted in 5% milk/TBST. The protein-antibody conjugates were detected using an enhanced chemiluminescence system. Protein expression, quantified using ImageJ software, was normalized to β-actin (ACTB) or glyceraldehyde-3-phosphate dehydrogenase (GAPDH). Western blots shown are representative of 3 independent experiments unless otherwise indicated in the figure legends. Details of the antibodies are listed in Table S3.

Proliferation and apoptosis assay

For the proliferation and apoptosis assay, cancer cells (A549 or H1650) were seeded at 6,000 cells/well in a 96-well plate and allowed to grow for 24 hours. They were then subjected to serum starvation for a further 24 hours. After starvation, cancer cells were incubated for 24 or 48 hours with different macrophage conditioned media (CM) and different metabolites or reagents as indicated in the results section. Proliferation and apoptosis were analyzed the next day using a bromodeoxyuridine (BrdU) cell proliferation assay kit and an ELISA-based cell death detection kit (both from Roche, Basel, Switzerland) according to the manufacturer's protocol.

Magnetic-activated cell sorting (MACS)

For MACS sorting of tumor associated macrophages (TAMs) from human lung tumors and normal tissue, single-cell suspensions were initially prepared. Human lung tumor single-cell suspensions were generated using the Tumor Dissociation Kit (Miltenyi Biotec, Germany) following the manufacturer's instructions. Mϕ isolation from these suspensions employed magnetic sorting with the human CD68-PE primary antibody (Miltenyi Biotec, Germany) and Anti-PE MicroBeads (Miltenyi Biotec, Germany), following the manufacturer's guidelines.

Flow cytometry and cell sorting

Single cell suspensions were prepared as described before and then blocked for 20 minutes with FcR blocking reagent (Miltenyi Biotec) in 0.5% PBS-BSA, stained with fluorochrome-conjugated antibodies and analyzed on a FACS Symphony A5SE flow cytometer (BD Biosciences). Live single cells were identified by FSC/SSC characteristics. Data were analyzed using FlowJo V10 (TreeStar). All antibodies and secondary reagents were titrated to determine optimal concentrations. Comp beads (BD) were used to compensate for single colors to create multicolor compensation matrices. Fluorescence minus one controls were used for gating. Device calibration was checked daily using Cytometer Setup and Tracking beads (BD Biosciences). The following antibodies were used: anti-Ly6C-Per-CP-Cy5.5, anti-CD80 PE (BD Biosciences), anti-CD45-VioBlue, anti-MHC-II-APC (Miltenyi Biotec), anti-F4/80-PE-Cy7, anti-CD206-FITC and anti-Ly6G-APC-Cy7 (BioLegend).

Metabolome measurement via LC-MS/MS

Quantification of Oxylipins by LC-MS/MS: All samples received 10 μl of an internal standard stock solution. Lipid extraction was performed using a two-phase liquid-liquid procedure in which ethyl acetate was added, the samples were shaken vigorously, centrifuged (10,000 g, 5 minutes, 4 °C) and the upper organic phase was collected. The extraction was repeated with ethyl acetate + 0.1 % formic acid. Extracted lipids were dried under a continuous nitrogen stream at vacuum pressure, then resuspended in 50/50 methanol/water (containing 100 ng/ml flufenamic acid as internal control). LC-MS/MS analysis was then performed for primary fatty acids and oxylipins.

The UPLC-MS/TS method was based on Wang et al.[56] with minor adjustments and used a reversed-phase separation on an Acquity UPLC BEH shield RP18 column (2.1 × 100 mm; 1.7 μm; Waters, Milford, USA) on an Agilent 1290 Infinity LC system (Agilent, Waldbronn, Germany). The mobile phase consisted of (A) ACN/water/acetic acid (60/40/0.02, v/v/v) and (B) ACN/isopropanol (50/50, v/v). The analytes were eluted over 5.8 minutes at a flow rate of 0.5 ml/ minute under gradient conditions. Mass spectrometry was performed on a QTrap 5500 mass spectrometer (Sciex, Darmstadt, Germany) with electrospray ionization in negative mode, using Analyst 1.6.2 and MultiQuant 3.0 (Sciex, Darmstadt, Germany) for data acquisition and analysis, respectively.

Quantification of TCA cycle metabolites: Cell samples were lysed in ice-cold 85% methanol (10 μl/mg) through two freeze-thaw cycles. Medium samples were processed unchanged. The resulting homogenate or culture medium was centrifuged (15,000 g, 5 minutes, 4 °C). An equal volume of supernatant spiked with isotope-labeled internal standards was collected and samples were evaporated to dryness in a ConcentratorPlus (Eppendorf, Wesseling-Berzdorf, Germany). Reconstitution was carried out in 50 μl water + 0.5 % formic acid, and subsequent analysis was performed by LC-MS/MS.

For liquid chromatography, an Agilent 1290 Infinity LC system with a Waters Acquity UPLC HSS T3 column (150 mm × 2.1 mm, 1.8 μm, Waters, Eschborn, Germany) at 40 °C was used. A gradient elution with 0.5 % formic acid in water (mobile phase A) and 0.5 % formic acid in methanol (mobile phase B) at a flow rate of 400 μl/ minute was used. The gradient conditions were 2 % B for 1.5 min, followed by a 3 minutes gradient to 100 % B and a purification and equilibration step, resulting in a total LC run time of 10 min. All samples were injected with a volume of 2.5 μl. Mass spectrometry was performed using a QTrap 5500 mass spectrometer (Sciex, Darmstadt, Germany) with an ESI TurboIonSpray source in negative ionization mode. Calibration curves were generated with authentic standards, and Analyst 1.6.2 and MultiQuant 3.0 (both from Sciex, Darmstadt, Germany) were used for data acquisition and analysis, respectively.

Quantification of itaconate: Samples were processed as mentioned above. Itaconate was analyzed by LC-MS/MS with the following set-up: An Agilent 1290 Infinity LC system was used with a Luna Omega PS C18 column (1.8 μm; 100 x 2.1 mm; phenomenex) and coupled to a QTrap 5500 mass spectrometer (Sciex, Darmstadt, Germany). The column compartment was set to 40 °C. A gradient elution (same mobile phases as above) was carried out at a flow rate of 400 μl/min with the following parameter: 0–1 min 0.1 % B, 1–4 min 80 % B, 4–6.5 min 99.9 % B, hold for 1 min, 7.5–8 min 0.1 % B, hold for 1.5 min. Injection volume was 5–8 μl.

Metabolic flux analysis

A Seahorse XFe96 flux analyzer (Seahorse Bioscience, Agilent Technologies, USA) was used to measure OCR and ECAR. For mitochondrial perturbation, 1.5 μM oligomycin, 1 μM FCCP and 0.5 μM rotenone/antimycin were added sequentially. The rate of glycolysis was determined by sequential addition of 1.5 μM oligomycin, 2 g/l D-glucose and 100 mM 2-deoxyglucose. The changes in OCR or ECAR after addition of the substrate were calculated relative to the rate before injection. The measuring substances (103015–100 for OCR and 103020–100 for ECAR) were purchased from Agilent Technologies, USA.

RNAseq analysis

For RNA-seq, RNA was isolated from macrophage and A549 cells using the miRNeasy micro Kit (Qiagen) combined with on-column DNase digestion (DNase-Free DNase Set, Qiagen) to avoid contamination by genomic DNA. The integrity of the RNA and library

preparation was checked using the LabChip Gx Touch 24 (Perkin – Elmer). 1 μg of total RNA was used as input for the SMARTer Stranded Total RNA Sample Prep Kit – HI Mammalian (Clontech). Sequencing was performed on the NextSeq500 instrument (Illumina) using v2 chemistry with a 1x75bp single-end setup. The resulting raw data were checked for quality, adapter content and duplication rates using FastQC (Available online at: http://www.bioinformatics.babraham.ac.uk/projects/fastqc). Trimmomatic version 0.39 was used to trim reads after a drop in quality below a mean value of Q15 in a window of 5 nucleotides. Only reads above 15 nucleotides were released for further analysis. The trimmed and filtered reads were aligned with STAR 2.7.3a against the Ensembl human genome, version hg38 (ensemble release 99), using STAR 2.7.3a with the parameter "—outFilterMismatchNoverLmax 0.1" to increase the maximum ratio of mismatches to mapped length to 10 %.[57] The number of reads aligned to genes was counted using the tool featureCounts 1.6.5 from the subread package.[58] Only reads that map at least partially within exons were allowed and aggregated per gene. Reads overlapping with multiple genes or aligned to multiple regions were excluded. Duplicate reads were removed using Picard 2.21.7 (Picard: A set of tools (in Java) for working with next generation sequencing data in the BAM format). Differentially expressed genes were identified using DESeq2 version 1.26.0.[59] Only genes with a minimum fold-change of +- 1.5 (log2 +-0.59), a maximum Benjamini-Hochberg-corrected *p-value* of 0.05 and a minimum combined mean of 5 reads were classified as significantly differentially expressed. The ensemble annotation was enriched with UniProt data (release 24.03.2017) based on Ensembl gene identifiers (activities at Universal Protein Resource (UniProt)).

To assess the polarization state of IRG1$^+$ Mϕ, we identified the top 250 differentially expressed genes (DEGs) in IRG1$^+$ versus IRG1$^-$ Mϕ using human lung adenocarcinoma single-cell RNA-seq data.[25] These DEGs were then compared with reference gene sets derived from Mϕ stimulated with IL-4 or with LPS+IFN-γ, as reported in our previous studies.[6,8,27] Genes upregulated in IL-4-treated Mϕ, representing anti-inf. or tumor-promoting states, were classified as pro-tumor markers, while genes induced by LPS + IFN-γ stimulation, corresponding to pro-infl. or tumor-suppressive states, were defined as anti-tumor markers. The relative enrichment of these markers among the top DEGs in IRG1$^+$ Mϕ was visualized Figure 1J.

Transcriptomics analysis

Sample distribution was analyzed using principal component analysis (PCA) with R package PCAtools v2.6.0. Input data comprised log2 scaled counts per million. For differential gene expression analysis, R package limma v3.50.0 was employed,[60] considering genes with adjusted *p-value*s < 0.05 as significantly expressed.

LC-MS/MS based quantitative proteomics

The LC-MS/MS-based quantitative proteomics analysis was performed as described previously.[61] Briefly, cell pellets were lysed in a buffer containing 0.1% ProteaseMax, 4 M urea, 50 mM ammonium bicarbonate, and 10% acetonitrile, followed by sonication, vortex mixing, and centrifugation. Protein concentrations were measured from the resulting supernatants. For each sample, 10 μg of protein was reduced (6 mM dithiothreitol, 37°C, 1 h), alkylated (22 mM iodoacetamide, room temperature, 30 min, in the dark), and subsequently digested overnight with trypsin (1:50 enzyme-to-protein ratio) at 37°C. The resulting peptides were purified using C18 plates and then dried. Tryptic peptides were labeled with TMT10plex reagents, incubated for 2 h at room temperature, quenched using hydroxylamine, combined, and dried again. Peptides were reconstituted in 2% acetonitrile/0.1% formic acid and analyzed on an EASY-nLC1000 system coupled to a Q Exactive Plus Orbitrap mass spectrometer. Peptide separation was carried out on a 50 cm C18 column using a 4%–26% acetonitrile gradient over 180 min. MS data were acquired in a data-dependent acquisition mode, with full MS scans (m/z 350–1600, resolution 140,000) followed by HCD fragmentation of the top 16 precursor ions (resolution 70,000). Raw data were processed using Proteome Discoverer v2.2 and searched against the human SwissProt database with Mascot. The search settings allowed for two missed cleavages, a precursor mass tolerance of 10 ppm, and a fragment mass tolerance of 0.05 Da. Oxidation (M), deamidation (N/Q), and N-terminal acetylation were included as variable modifications. Quantification relied on unique and razor peptides. Downstream analyses were conducted in R. The data was normalized using the quantile method with the R package NormalyzerDE v1.12.0,[62] and this normalization was chosen for the subsequent analysis. Principal component analysis (PCA) was performed using the R package PCAtools v2.6.0 with default settings. For differential expression analysis, the R package limma v3.50.0 was used, and proteins with adjusted p-values < 0.05 were considered significantly expressed.

Integrative analysis

Weighted co-expression network analysis was performed separately for proteomics and transcriptomics data. Quantile-normalized data served as input for the proteomics network analysis, with proteins with a variance of less than 0.01 removed prior to analysis. Spearman correlations between proteins were calculated, and significant correlations (adjusted p-values < 0.05) were used to construct the co-expression network. For transcriptomics network analysis, data were normalized to transcripts per million (TPM), and genes with a variance of less than 0.1 were removed. Significant correlations (adjusted p-values < 0.05) between genes were used to construct the co-expression network. The constructed networks were analyzed using igraph, with the spearman correlation coefficient serving as the edge weight. Coexpression communities were identified by modularity maximization using the Leiden algorithm.[63] The centrality of the communities was calculated by averaging the degree centrality of the nodes within each community. Functional analysis of co-expression communities was performed using the enrichr module of gseapy v0.10.5,[64,65] with Hallmark gene sets v7.5.1 from the Molecular Signatures Database (MSigDB) as reference. Significantly enriched gene sets (adjusted p-values< 0.05) for each community in both proteomics and transcriptomics networks were selected to assess functional overlap. Fisher's exact test was used to find functional relationships between community pairs, where relationships with adjusted

p-values < 0.1 for macrophage data and adjusted p-values < 0.05 for A549 data were considered significant for defining functional similarity between proteomics and transcriptomics co-expression landscapes. Volcano plots and sankey plots were generated using R package ggplot2 v3.3.5. Heatmaps were created using R package ComplexHeatmap v2.10.0.[66] Bubble plots were created using Cytoscape v3.6.1.

Olink assay

The Olink Target 96 panels use proximity extension assay technology for the simultaneous analysis of 92 biomarkers with 1ul of cell lysate prepared using RIPA buffer. The target proteins bind to antibody pairs with coupled DNA oligonucleotides, resulting in hybridization and extension by DNA polymerase and generating double-stranded DNA barcodes. These barcodes are amplified and quantified by microfluidic real-time PCR. Strict quality control and normalization with internal controls minimize variation within and between tests. Results are reported as Normalized Protein eXpression (NPX) values on a log2 scale.

G6PD enzyme activity

For the preparation of tissue sections, lung tissue was deep-frozen and cut into 6 μm sections on superfrost slides. Sections were stained using a G6PD-specific enzymatic assay as previously described.[67] Sections were incubated with a G6PD-specific reaction medium containing glucose-6-phosphate (G6P), $NADP^*$, $MgCl_2$, sodium azide, methoxyphenazine, and nitroblue tetrazolium chloride (NBT). Active G6PD generates NADPH from G6P, which in turn reduces NBT via methoxyphenazine, forming a purple formazan precipitate at sites of enzyme activity. The reaction medium was applied directly to the tissue and incubated at room temperature until a distinct purple color developed (approximately 1–2 minutes). After the stability of color, the reaction was then stopped by removing the medium and washing slides with warm PBS. Negative control reactions were performed without substrate or in the presence of 80 mM dehydroepiandrosterone as a G6PD inhibitor. Bright-field images were acquired, and the intensity of the formazan signal was quantified using ImageJ (8-bit conversion, automatic threshold, and measurement of area, area fraction, and mean gray value). For cell lysate, G6PD activity was determined spectrophotometrically as described.[67] Lung cancer cells or Mϕs were sonicated and the protein concentration of the supernatant was measured. G6PD activity was determined in the presence of $MgCl_2$, $NADP^+$ and different concentrations of G6P. Reactions were initiated by addition of cell supernatant or recombinant G6PD (ab167987, abcam), and enzyme activity was measured for 20 minutes at room temperature using a TECAN infinite M200 pro plate reader in kinetic mode at 340 nm.

Stable isotope tracing with 1,2-$^{13}C_2$-Glucose

A549 lung cancer cells were cultured under standard conditions (37 °C, 5% CO_2) in complete medium containing 10% fetal calf serum (FCS) and 1% penicillin-streptomycin. For each experimental condition, 2×10^6 cells were plated per well. Four biological replicates were prepared for each treatment group, including untreated controls. Cells were pre-treated for 24 hours with either Octyl Ita in complete medium. Following treatment, the medium was replaced with glucose-free DMEM supplemented with 1,2-$^{13}C_2$-glucose at 4.5 g/L for A549 cells, and Octyl Ita. Labeling was performed for 3 hours, after which cell culture plates were immediately placed on dry ice and culture supernatants was removed. Cells were rapidly washed with ice-cold deionized water, which was then completely removed. Metabolites were extracted by adding 1.5 mL of pre-cooled 85:15 methanol/water. Cells were scraped on ice, and the extracts were transferred to microcentrifuge tubes, vortexed, incubated on ice for 5 min, vortexed again, and centrifuged at 16,000 × g for 20 min at 4 °C. The supernatants were transferred to new tubes, dried and stored at −80 °C until further analysis. Prior to LC–MS analysis, samples were taken up in 300 μL buffer (80% Methanol, 25 mM Ammonium Acetate and 2.5 mM Na-Ascorbate prepared in LC-MS water, supplemented with isotopically-labelled amino acid standards [Cambridge Isotope Laboratories, MSK-A2-1.2], aminopterin, and reduced glutathione standard [Cambridge Isotope Laboratories, CNLM-6245-10]). Samples were vortexed for 10 sec, then centrifuged for 10 minutes at 18,000g to pellet cell debris. The supernatant was dried on ice using a liquid nitrogen dryer. Metabolites were reconstituted in 20 uL water and 1 uL was injected into a ZIC-pHILIC 150 x 2.1 mm (5 um particle size) column (EMD Millipore) operated on a Vanquish Duo UHPLC Systems (Thermo Fisher Scientific, San Jose, CA, USA). Chromatographic separation was achieved using the following conditions: buffer A was acetonitrile; buffer B was 20 mM ammonium carbonate, 0.1% ammonium hydroxide in water. Gradient conditions were: linear gradient from 20% to 80% B; 20–20.5 min: from 80% to 20% B; 20.5–28 min: hold at 20% B at 150 mL/min flow rate. The column oven and autosampler tray were held at 25 °C and 4 °C, respectively. MS data acquisition was performed using a Thermo Exploris 480 benchtop orbitrap mass spectrometer equipped with an EASY-IC ion source and a high flow HESI probe (Thermo Fisher Scientific, San Jose, CA, USA) and was performed in positive and negative ionization mode in a range of m/z = 70–1000, with the resolution set at 70,000, the AGC target at 1×10^6, and the maximum injection time (Max IT) at 20 msec.

Relative quantification of polar metabolites was performed with Compound Discoverer (CD) 3.4 implementing in-house libraries (470 compounds and 37 internal standards). A general workflow was built to best suit our polar metabolomics LC-MS method. Positive and negative modes were analyzed together. Filtering steps were performed based on peak noise levels, ppm error, formula annotation, and the relative abundance of the integrated peak area in true sample compared to blank injections, where features with -+>3-fold higher in samples were retained. Within our HILIC chromatography, we rarely observe chromatographic shifts larger than 1 minute and retention times drifts larger than 60 seconds, thus these parameters were set as limits for retention time correction and matching to internal databases. Pooled samples and fractional dilutions were prepared as quality controls and injected at the beginning and end of each run. In addition, pooled samples were interspersed throughout the run to control for technical drift in signal

quality as well as to serve to assess the coefficient of variability (CV) for each metabolite. Post CD, data was further consolidated with an in-house R script (https://github.com/FrozenGas/KanarekLabTraceFinderRScripts/blob/main/MS_data_script_v2.4 _20221018.R). This script: 1) extracts and combines the peak areas from CD output.csvs; 2) calculates and normalizes to an averaged factor from all mean-centered chromatographic peak areas of isotopically labeled amino acids internal standards within each sample; 3) reports on low-quality metabolites based on user inputted cut-offs calculated from pool reinjections and pool dilutions. In this study, the linear correlation between the dilution factor and the peak area cut-offs are set to RSQ>0.95 and the coefficient of variation (CV) < 30%. Finally, data were Log transformed and Pareto scaled within the MetaboAnalyst-based statistical analysis platform[68] to generate PCA, PLSDA, volcano plots and heatmaps.

Isotope tracing data were analyzed using a combination of Compound Discoverer (CD) 3.4 and TraceFinder (TF) 5.2. In CD, compounds were identified using the same workflow as for targeted metabolomics, except that isotopologue peak areas were calculated individually rather than summed. Isotope abundance correction was performed automatically within CD. For identification of ^{13}C-labeled metabolites in TF, the expected m/z values were generated by adding the mass of an additional proton (m = 1.00727) for each potential labeled carbon of a compound of interest. Peak areas were automatically computed and verified manually. Post TF, natural ^{13}C abundance was corrected using the R package IsoCorrectoR.[69] Corrected abundances from TF or CD were reported either as the change in percent labeling between experimental conditions, as absolute pool sizes, or as absolute abundances per isotopologue. For absolute comparisons, peak areas were normalized, as in targeted analysis, to an averaged factor derived from mean-centered peak areas of QC-passing metabolites per sample ($R^2 > 0.95$; CV < 30%).

MALDI-MSI Sample Preparation and Data Acquisition

Mouse lung tissue samples were harvested immediately after euthanasia of the mice and embedded freshly in gelatin 8%–10% on top of dry ice then stored at –80 °C until further processing. Cryosections (10–12 μm thick) were prepared at –20 °C using a Thermo CryoStar NX50 cryostat and thaw-mounted onto IntelliSlide (Bruker Daltonics). Sections were then desiccated under vacuum for at least 30 minutes to remove residual moisture and improve matrix adherence. Matrix coating was performed using 1,5-diaminonaphthalene (DAN), prepared at a concentration of 10 mg/mL in a 70:30 (v/v) acetonitrile:water solution. The matrix was uniformly applied using an HTX M3+ Sprayer (HTX Technologies, USA) under the following conditions: 8 passes, flow rate of 70 μL/min, nozzle temperature of 70 °C, and track spacing of 2 mm and 10psi N2 pressure.[70] Mass spectrometry imaging was performed using a Bruker TimsTOF fleX MALDI-2 instrument operating in negative ion mode. Spectra were acquired over a mass-to-charge (m/z) range of 50–650, with a spatial resolution of 20 μm per pixel, enabling high-resolution molecular imaging. Each pixel spectrum was generated by accumulating 200 laser shots. External calibration was conducted prior to acquisition using red phosphorus together with online calibration for taurine and palmitate, ensuring accurate m/z assignment throughout the dataset.

Raw MALDI imaging data were imported into SCiLS Lab 2025b Core software (Bruker Daltonics, Bremen, Germany) for preprocessing. Root Mean Square (RMS) normalization were uniformly applied across all datasets to minimize technical variability and enable robust inter-sample comparisons. Unsupervised segmentation was carried out using bisecting k-means clustering in SCiLS Lab to identify spatially distinct molecular regions. These were aligned with corresponding hematoxylin and eosin (H&E)-stained images obtained from the same tissue sections.[71] MALDI data were processed using the MetaboScape 2025 platform (Bruker Daltonics). For metabolite annotation, detected m/z features were cross-referenced with available databases using a target list derived from the Bruker NIST 2020 MS/MS Spectra Library and the MS-DIAL Tandem Mass Spectra Atlas (VS69). Annotation was further refined by applying defined search parameters, including m/z tolerance and mSigma, to ensure accurate feature matching. The results were first exported in.mca format to SCiLS Lab for peak width refinement and ion image quality assessment.

G6PD modification with ITalk

A549 lung cancer cell were treated with ITalk (250μM) for 6 hours. Then, proteins were extracted by 4% SDS, 100mM Tris, ph7,6 with protease inhibitors. Isolated proteins were solubilized with Laemmli SDS sample buffer and separated by polyacrylamide electrophoresis (NuPAGE 4–12% Bis-Tris gel, Thermo Fisher Scientific). G6PD corresponding gel lanes were cut and subsequently reduced (10 mM dithiothreitol) and alkylated (55 mM iodoacetamide), followed by overnight digestion using trypsin (Serva). Tryptic peptides were eluted from the gel by gradient of acetonitrile. Digested proteins were desalted using a C18 stage tip. Digested proteins were desalted using a C18 stage tip. Desalted peptides were measured by LC-MS/MS. Quantitative analyzes were performed on an Orbitrap Q-exactive HF mass spectrometry system (Thermo Scientific) coupled to an EASY-nLC capillary nano-chromatography system (Thermo Scientific) as previously described.[72] Desalted peptides were separated on an in-house-made capillary column (150 mm x 1.7 μm x 75 μm) packed with ReproSil-Pur 120 C18-AQ resin (Dr. Maisch). The mobile phases were (A) 2% Acetonitrile, 0.1% fomic acid (B) 90% acetonitrile, 0.1% formic acid. Peptides were separated using a 150-minute acetonitrile gradient at room temperature. The mass spectrometer was operated in positive electrospray ionization (ESI) mode, and MS/MS data were collected in data dependent analysis mode with a resolution of 60,000 for precursor mass spectra and 15000 for tandem mass spectra. Normalized collision energy was set to 28 and exclusion time was set to 30s. Collected data were processed using Maxquant software and verified manually.

GSH/GSSG measurement

A549 cells were seeded at 0.1×10^6 cells per ml in opaque 96-well plates. Cells were treated with Octyl Ita (250 μM) for 6 hours, then the cell supernatant was removed and the ratio of reduced glutathione to oxidized glutathione (GSH/GSSG) was quantified using the

Promega GSH/GSSG-Glo assay (V6611) according to the manufacturer's instructions. Luminescence was quantified using a TECAN infinite M200 pro plate reader.

In silico analysis of G6PD activity

Ligand preparation: itaconic acid were sketched using Marvin sketch and saved as MOL files for molecular docking. Energy minimization was performed using PyRx and structures were visualized with Marvin view. Selected ligands were converted into 3D structures using Biovia Discovery software. Preparation of the proteins: The 3D structure of G6PD dehydrogenase (PDB ID: 2BHL) was retrieved from the PDB database, and polar hydrogens were added using Discovery Studio Visualizer. Molecular docking analysis: the active site of G6PD contained β-D-glucopyranose-6-phosphate as a reference ligand. AutoDock Vina, a reliable docking program, was used for the analysis. The hydrogen bonding interactions of itaconate in the active site and the docking scores (ΔG; kcal/mol) were determined.

Precision cut lung slices from human lung cancer patients

For tumor-derived precision-cut lung slices (TD-PCLS) preparation, freshly resected human lung lobes with tumors were infused with 1% low-melting agarose (A9414, Sigma, USA) in DMEM/F12 medium. Proliferation and apoptosis rates in TD-PCLS were determined using EdU and Tunel assays as previously described.[27,73]

Immunofluorescence staining

Frozen tissue sections and fresh TD-PCLS were used for immunofluorescence staining (IF). The tissue sections were first fixed with 4 % PFA, permeabilized with 0.3 % Triton X-100, blocked with 5 % BSA and then stained with primary and secondary antibodies according to the usual protocol. For IF staining of mouse lung tumors, images was randomly collected from each mouse. To ensure statistical power, at least three mice were included in each experimental group, with selection criteria based on the number of tumor nodules observed in the entire lung section.

Tumor cell injection

In the subcutaneous (s.c) tumor model, C57BL/6 mice were injected with 1×10^6 mouse LLC1 cells using a 24 g needle. Tumor growth was monitored every 4 days, and on day 16, mice were euthanized for tumor removal. In the intravenous injection model, LLC1 cells (1×10^6) were injected into C57BL/6 or *Irg1*$^{-/-}$ mice via the tail vein, and all mice were closely monitored for 17 days.[8,74] μCT (Bruker Skyscan 1276) imaging was performed one day before sacrifice. The effect of Octyl Ita on tumor growth was examined by intraperitoneal administration of 100 mg/kg every other day for 10 days for s.c model and 2 weeks for i.v. model, starting 4 days after tumor induction, using 2-hydroxypropyl-beta-cyclodextrin as vehicle for both Octyl Ita and placebo groups.

Bone marrow transplantation (BMT)

C57BL/6 recipient mice were irradiated once using the RS-2000 Biological Irradiator. They then received an intravenous transfer of 1.5–2x10^7 bone marrow cells from *Irg1*$^{-/-}$ donor mice. After 21 days of bone marrow reconstitution, the mice were given a further 10 days of rest before receiving an injection of 10^6 LLC1 cells into the tail. On day 18 based on the overall health and welfare status, the mice were euthanized and their tumors were removed.

QUANTIFICATION AND STATISTICAL ANALYSIS

Quantification

Quantification of western blot and staining data was carried out using ImageJ. MALDI imaging data were processed and analyzed with SCiLS Lab, as detailed in the respective sections.

Statistical analysis

The statistical analysis was performed using Prism 9 software (GraphPad Software Inc., San Diego, USA). A two-tailed Student's t-test was used to compare two groups. For more than two groups, differences were assessed using a one-way or two-way ANOVA multiple comparison test. Data are presented as mean ± S.E.M.